INL/JOU-21-65135-Revision-1



# Microstructural Development in Inconel 718 Nickel-Based Superalloy Additively Manufactured by Laser Powder Bed Fusion

January 2022

Thinh Huynh, Nicolas E Woolstenhulme, Devin D Imholte, Daniel M Wachs

Changing the World's Energy Future


*INL is a U.S. Department of Energy National Laboratory operated by Battelle Energy Alliance, LLC*

INL/JOU-21-65135-Revision-1

# Microstructural Development in Inconel 718 Nickel-Based Superalloy Additively Manufactured by Laser Powder Bed Fusion

**Thinh Huynh, Nicolas E Woolstenhulme, Devin D Imholte, Daniel M Wachs**

**January 2022**

**Idaho National Laboratory**
**Idaho Falls, Idaho 83415**

**http://www.inl.gov**

**Prepared for the**
**U.S. Department of Energy**
**Under DOE Idaho Operations Office**
**Contract DE-AC07-05ID14517**

# Microstructural Development in Inconel 718 Nickel-Based Superalloy Additively Manufactured by Laser Powder Bed Fusion

[a]Thinh Huynh, [a]Abhishek Mehta, [a]Kevin Graydon, [a]Jeongmin Woo, [a,1]Sharon Park, [a,2]Holden Hyer, [a,3]Le Zhou, [b]D. Devin Imholte, [b]Nicolas E. Woolstenhulme, [b]Daniel M. Wachs, [a,]*Yongho Sohn

[a] Department of Materials Science and Engineering
University of Central Florida, Orlando, FL 32816, USA

[b] Nuclear Fuels and Materials Division
Idaho National Laboratory, Idaho Falls, ID 83415, USA

[1] Now at Department of Materials Science and Engineering, Johns Hopkins University, Baltimore, MD, USA

[2] Now at Oak Ridge National Laboratory, Oak Ridge, TN 37830, USA

[3] Now Assistant Professor, Department of Mechanical Engineering, Marquette University, Milwaukee, WI 53233, USA.

*Corresponding authors

Yongho Sohn, Ph.D., FASM
UCF Pegasus Professor and Lockheed-Martin Professor of Engineering
Advanced Materials Processing and Analysis Center
Department of Materials Science and Engineering
University of Central Florida, Orlando, FL 32816, USA
Phone: 407-882-1181; Email: yongho.sohn@ucf.edu

## Abstract

Excellent weldability and high temperature stability make Inconel 718 (IN718) one of the most popular alloys to be produced by additive manufacturing. In this study, we investigated the effects of laser powder bed fusion (LPBF) parameters on the microstructure and relative density of IN718. The samples were fabricated with independently varied laser power (125 - 350W), laser scan speed (200 - 2200 mm/s), and laser scan rotation (0° - 90°). Archimedes' method, optical microscopy, and scanning electron microscopy were employed to assess the influence of LPBF parameters on the relative density and microstructure. Optimal processing windows were identified for a wide range of processing parameters and relative density greater than 99.5% was achieved using volumetric energy density between 50 and 100 J/mm$^3$. Microstructural features including melt pool geometry, lack of fusion defect, keyhole porosity, and sub-grain cellular microstructure were examined and quantified to correlate to LPBF parameters. A simple empirical model was postulated to relate relative sample density and LPBF volumetric energy density. Melt pool dimensions were quantitatively measured and compared to estimations based on Rosenthal solution, which yielded a good agreement with the width, but underestimated the depth, particularly at high energy input, due to lack of consideration for keyhole mode. In addition, the sub-grain cellular-dendritic microstructure in the as-built samples was observed to decrease with increasing laser scan speed. Quantification of the sub-micron cellular-dendritic microstructure yielded estimated cooling rate in the order of $10^5 – 10^7$ K/s.

## 1. Introduction

Laser powder bed fusion (LPBF), also known as selective laser melting (SLM) utilizes laser to melt selective regions of a powder bed, layer by layer, corresponding to the sliced model of a computer-generated design. Since the rapid movement of the laser is accompanied by a very rapid solidification/cooling ($10^3$ – $10^8$ K/s) [1,2], nearly unlimited geometrical complexity and customization can be adopted to produce near net-shape components.

Traditional manufacturing techniques such as casting, forging, and powder metallurgy has been established for manufacturing of Inconel 718 (IN718) [3,4]. However, recent advancements in metal additive manufacturing (AM) enabled rapid production of complex geometries while providing design freedom for customized components [5,6]. Since it is impractical to work harden components produced via LPBF, precipitation strengthened alloys such as IN718 received spotlights in AM technologies. While rapid solidification [7-9] and directional cooling [10-12] influence the as-built microstructure [13-16] and phase transformations [17-19], repeated thermal cycling adds another layer of complexity. Extreme cooling rates as high as $10^8$ K/s can induce constitutional supercooling ahead of the solidification front, which result in the instability of the solid-liquid interface [20,21]. Consequently, the non-planar solidification will assume cellular or dendritic morphologies [22]. The as-printed microstructure of IN718 consists of a matrix of fine cellular dendrites [23-25]. Simulations mimicking solidification conditions of IN718 showed segregation of strengthening elements along the intercellular or interdendritic regions [26].

Based on transmission electron microscopy, Zhou *et* al. [27] demonstrated that the as-built microstructure was dominated by segregation of Niobium (Nb), Molybdenum (Mo), and Titanium (Ti) along the cellular boundaries and interdendritic regions. Moreover, nano-scaled Laves in the form of $(Ni,Cr,Fe)_2(Nb,Mo,Ti)$ and carbides including (Nb,Ti)(C,B) at 100 – 200 nm, and 50 nm,

respectively, were observed in the as-built condition along the interdendritic regions with significant microsegregation. This is similar to that observed in a greater magnitude for wrought and cast material [28].

Over the past decade, researchers have focused on many aspects of microstructure and mechanical performance of IN718 [29-36]. Optimizing the processing parameters of LPBF can be quite arduous. Generally, the most influential processing parameters include laser power, laser scan speed, laser hatch spacing, and slice thickness. To understand the influence of these processing parameters on the relative density and microstructure, a normalized volumetric energy density can be adopted [1,2] and is defined as:

$$\text{Energy Density (ED)} = \frac{\text{Laser Power}}{\text{Laser Scan Speed} \times \text{Hatch Spacing} \times \text{Slice Thickness}} \quad (1)$$

Despite numerous studies on this nickel-base superalloy, limited efforts were made to comprehensively document the influence of processing parameters. The mechanical properties of AM'ed IN718 has been widely explored in literature, and a previous publication [27] detailing the correlation between microstructure and mechanical properties was completed. Thus, it is imperative to investigate how the variation in LPBF parameters can influence IN718 microstructure manufactured by LPBF. This work was carried out to correlate the LPBF parameters of IN718 with the relative density and microstructure. Estimation of cooling rates were also carried out using simple models available for solidification microstructure, and traditional welding to establish the trend between cooling rates and LPBF parameters.

## 2. Materials and Methods

### *2.1 Powder characterization*

Commercial IN718 powder feedstock for the LPBF was procured from SLM Solutions Group AG (Lubeck, Germany) with the average particle diameter of 45 μm. The particle size distribution was further examined using laser diffraction particle size analyzer (Beckman Coulter LS$^{TM}$ 13 320). Powder morphology and microstructure were observed using a field emission scanning electron microscope (FE-SEM, Zeiss Ultra-55$^{TM}$). As-received powders were mounted in epoxy resin and metallographically polished down to 0.25 μm diamond paste and etched using a mixed acid etchant for cross-sectional analysis. The etchant consisted of hydrochloric acid (HCl), acetic acid ($CH_3COOH$), and nitric acids ($HNO_3$) at a volumetric ratio of 3:2:1, respectively. Powder circularity and cross-section microstructure were examined using optical microscope (Nikon Metaphot) and SEM, respectively. Chemical composition analysis of the powders was conducted using X-ray energy dispersive spectroscopy (XEDS) equipped on FE-SEM and compared to the chemistry standard ASTM F3055-14 reported in Table 1. Quantification of individual/overall powder density was carried out using image processing and analysis software (ImageJ$^{TM}$, NIH) from ten randomly selected areas.

Table 1: Composition (wt.%) of IN718 powder feedstock from XEDS and ASTM F3055 - 14.

| | Ni | Cr | Fe | Nb | Mo | Co | Ti | Al | Si | Mn |
|---|---|---|---|---|---|---|---|---|---|---|
| **XEDS** | 51.27 (±0.59) | 20.44 (±0.18) | 18.85 (±0.59) | 4.57 (±0.59) | 2.52 (±0.21) | 0.09 (±0.17) | 1.02 (±0.16) | 1.03 (±0.20) | 0.15 (±0.09) | 0.06 (±0.09) |
| **ASTM** | 50.0 ~ 55.0 | 17.0 ~21.0 | 17.0 | 4.75 ~ 5.5 | 2.8 ~ 3.3 | 1.00 | 0.65 ~ 1.15 | 0.20 ~ 0.80 | 0.35 | 0.35 |

### *2.2 Laser powder bed fusion and specimen preparation*

An SLM 125$^{HL}$ (SLM Solutions Group AG Lubeck, Germany) LPBF system, equipped with a single continuous-wave (1070 nm) IPG fiber laser was employed to print cubic samples with dimensions of 10 x 10 x 10 mm. All samples were fabricated on an IN718 substrate pre-heated to 100 °C and within an argon atmosphere containing an oxygen content below 0.1 %. The most influential processing parameters including laser power, laser scan speed, and laser scan rotation were varied independently to examine the formation of defects and microstructure. The processing parameters were varied systematically around the optimized parameter set obtained from SLM Solutions specifications in which the laser power, scan speed, slice thickness, hatch spacing, and scan rotation angle is 200 W, 900 mm/s, 0.03 mm, 0.12 mm, and 67°, respectively.

In order to observe the melt-pool characteristics in LPBF, initial layer rotation was adjusted to ensure that the last melt-pool is perpendicular to the XZ plane. After fabrication, the samples were removed from the substrate *without* standard stress relieving (ASTM F3055). Lateral and bottom surfaces of the samples were ground using silicon carbide (SiC) paper to minimize surface bubbles during density measurements via immersion technique. Relative density measurements of the printed samples were conducted via Archimedes' method, pursuant of ASTM B962 - 17. The samples were cross sectioned parallel to the build direction (XZ) and perpendicular to the build direction (XY), with the z-axis along the build direction. All sample surfaces were metallographically polished down to 0.25 μm diamond paste using standard metallographic procedures and etched using the above-mentioned etchant for 30 – 60 sec.

### *2.3 Microstructural characterization*

Microstructures before and after chemical etching were examined using optical microscopy and SEM, respectively. Prior to etching, the porosity in each sample were quantified via image

analysis, and the average relative density was estimated by assuming the area fraction of defects was equal to the volume fraction. To ensure statistical confidence, relative density was determined using 10 optical micrographs at 50X magnification. After chemical etching, the melt pool depth and width of the last melted layer (e.g., top of the sample) for each sample were obtained via image analysis. Melt pool dimensions were acquired using the measurement technique illustrated in Figure 1. Assuming parabolic symmetry, the actual melt pool widths were approximated to be twice the measured width. Statistical variation in the melt pool dimensions were estimated using 5 random optical micrographs at 50X magnification. Quantification of the cellular microstructure using the linear intercept method, pursuant of ASTM E112 – 13, was conducted via image analysis. Chemical composition of the segregated microstructure was obtained using XEDS on FE-SEM.

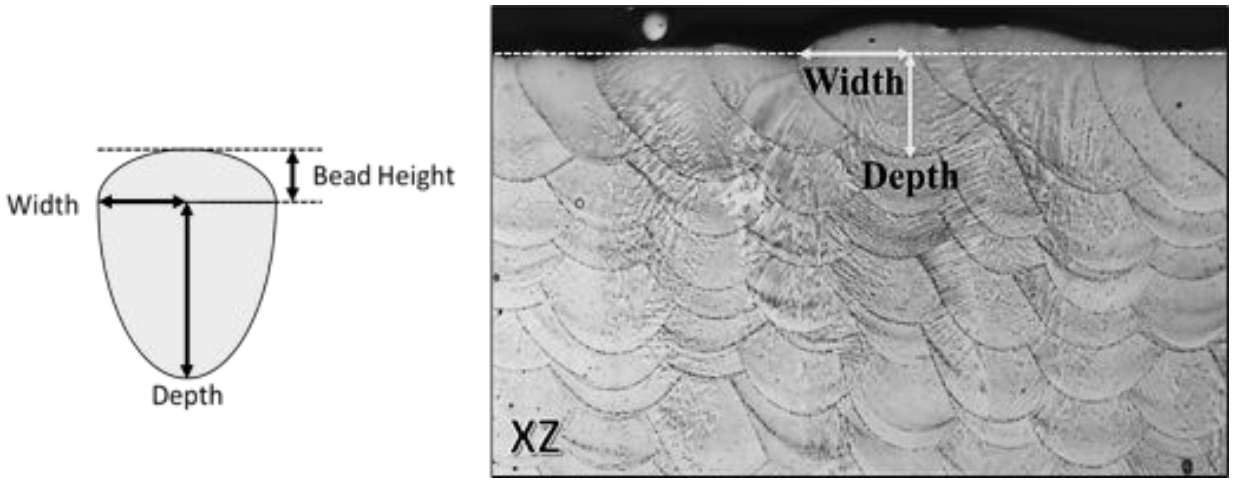


Figure 1: A schematic and representative optical micrograph of melt pools showing lateral symmetry. Note that the actual melt pool width is twice that of measured width indicated.

## 3. Results and Discussion

### *3.1 Powder feedstock morphology and microstructure*

Typical composition of IN718 powders is reported in Table 1. Figure 2 presents that the mean particle size of the powder feedstock was 32.90 µm, and 90 percent of the distribution lied below 44.26 µm. Cross-sectional optical micrograph of IN718 powders, presented in Figure 3(a), demonstrates that the powders were highly circular with negligible internal porosity. Quantification of the powder circularity and powder density yielded 0.88 ± 0.01 and 99.98 ± 0.02 %, respectively. Figure 3(b) illustrates the overall spherical nature of the powders with limited satellite formation around the powder surface. The backscatter electron (BSE) images in Figures 3(c) and 3(d) indicate elemental contrast of the dendritic microstructure. Compositional analysis reported in Table 2 suggested that the cellular boundaries (point 2) to be enriched in Nb, Ti, and Mo as compared to the primary γ matrix (point 1).

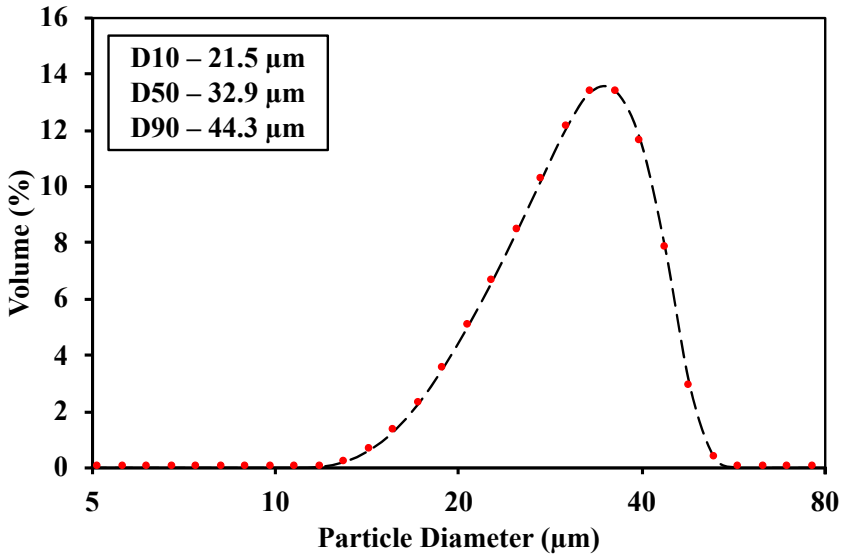


Figure 2: Particle size distribution of as-received IN718 powder feedstock.

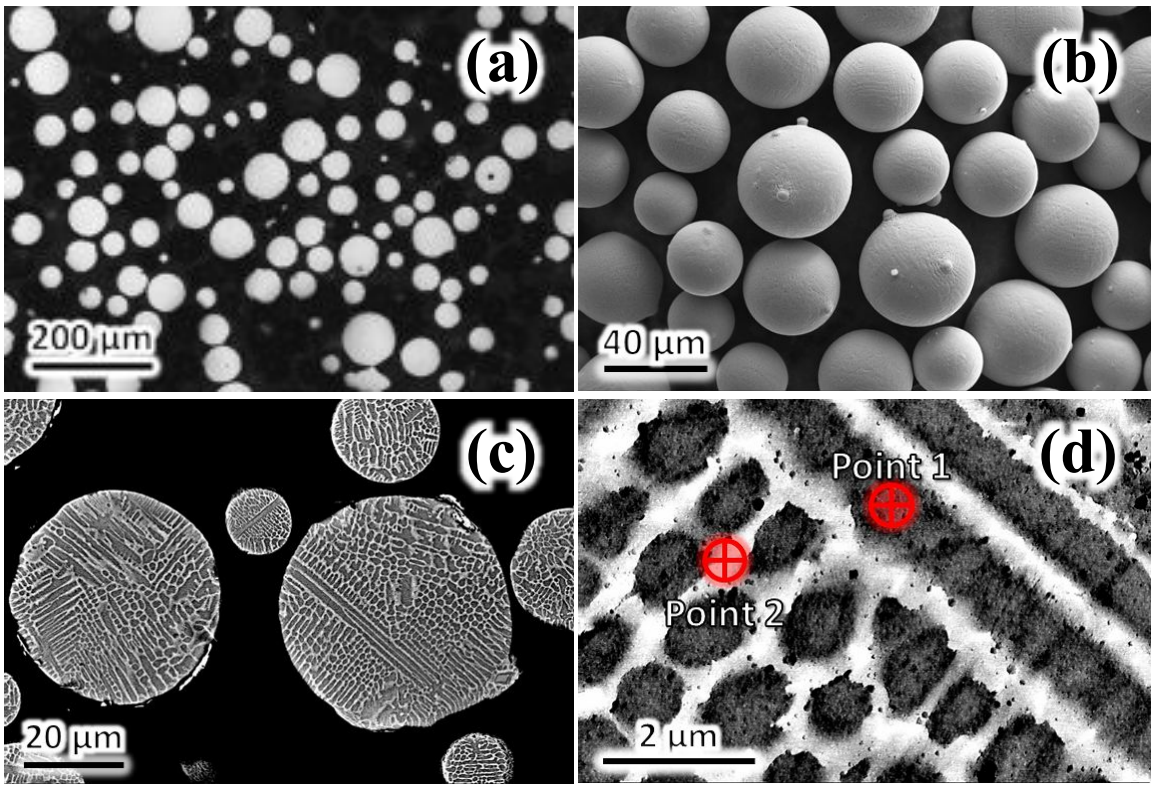


Figure 3: (a) Optical micrograph of unetched IN718 powder cross section, (b) secondary electron (SE) micrograph of IN718 powder, (c) backscatter electron (BSE) micrograph of IN718 powder, (d) cellular-dendritic microstructural details in SE micrograph.

Table 2: XEDS composition (wt.%) from regions of interests identified in Figure 3(d) from IN718 powder feedstock.

| | Ni | Cr | Fe | Nb | Mo | Co | Ti | Al | Si | Mn |
|---|---|---|---|---|---|---|---|---|---|---|
| **Point 1** | 51.68 (±0.53) | 19.54 (±0.21) | 18.65 (±0.19) | 7.47 (±0.27) | 1.29 (±0.22) | -- | 0.67 (±0.06) | 0.39 (±0.07) | 0.31 (±0.06) | -- |
| **Point 2** | 48.34 (±0.51) | 18.01 (±0.21) | 15.82 (±0.18) | 14.24 (±0.30) | 1.92 (±0.25) | 0.06 (±0.06) | 1.12 (±0.06) | 0.16 (±0.07) | 0.32 (±0.06) | -- |

### *3.2 Effect of laser power and scan speed on defect formation*

To explore the effects of laser power and laser scan speed on the relative density of IN718 samples, optical micrographs were utilized for image analysis to estimate the sample density over a wide range combinations of laser powers and laser scan speeds. As shown in Figure 4, samples with slow laser scan speeds had mostly circular porosity induced by keyhole melting. As the laser scan speed increased, a clear departure from circular pores was observed. At a constant laser power, an

increase in laser scan speed was accompanied with a transition from low-density to high-density samples. When the laser scan speed exceeded the high-density threshold, a lower density microstructure appeared with irregularly shaped lack-of-fusion flaws. While the transition of defect formation characteristic remained similar across all investigated laser powers, samples fabricated with higher laser powers had more gradual transitions from low-density to high-density regions. In other words, the LPBF processing window that produced higher relative density for IN718 was observed to be larger when fabricated with 275 W and 350 W. Overall trend in sample density (or pores/flaws) is presented in Figure 5 as functions of laser power and scan speed.

Optical micrographs in Figures 4 and 5 clearly display the transition from circular pores to high part density, and finally to irregularly-shaped flaws. The normalized volumetric energy density input ultimately affects the melting, fluid flow, and solidification process during laser-material interaction. As the energy density increases, the powder bed become excessively molten and subsequent vaporization of the material results in a cavity filled with vapor or plasma [37]. Upon solidification, collapse of the keyhole melt pools proceeds when the aggressive vapor pressure is lower than ambient pressures [38]. Consequently, at very high energy density, rapidly solidifying walls prevent the vapor-filled cavity from escaping the deep fluctuating keyholes during mechanical collapse [39]. When the laser absorption is insufficient in maintaining the required recoil pressure, the more dominant surface tension driven by the Marangoni effect would keep the liquid surface as small as possible and prevent the occurrence of a keyhole [40]. In direct contrast, a very low energy density resulted in a clear engagement of conduction mode. The powder bed is melted by heat conduction effects at higher laser scan speeds, and the shape of conduction mode melt pools is controlled by thermal conduction [41], which explains the appearance of irregular or lack of fusion defects.

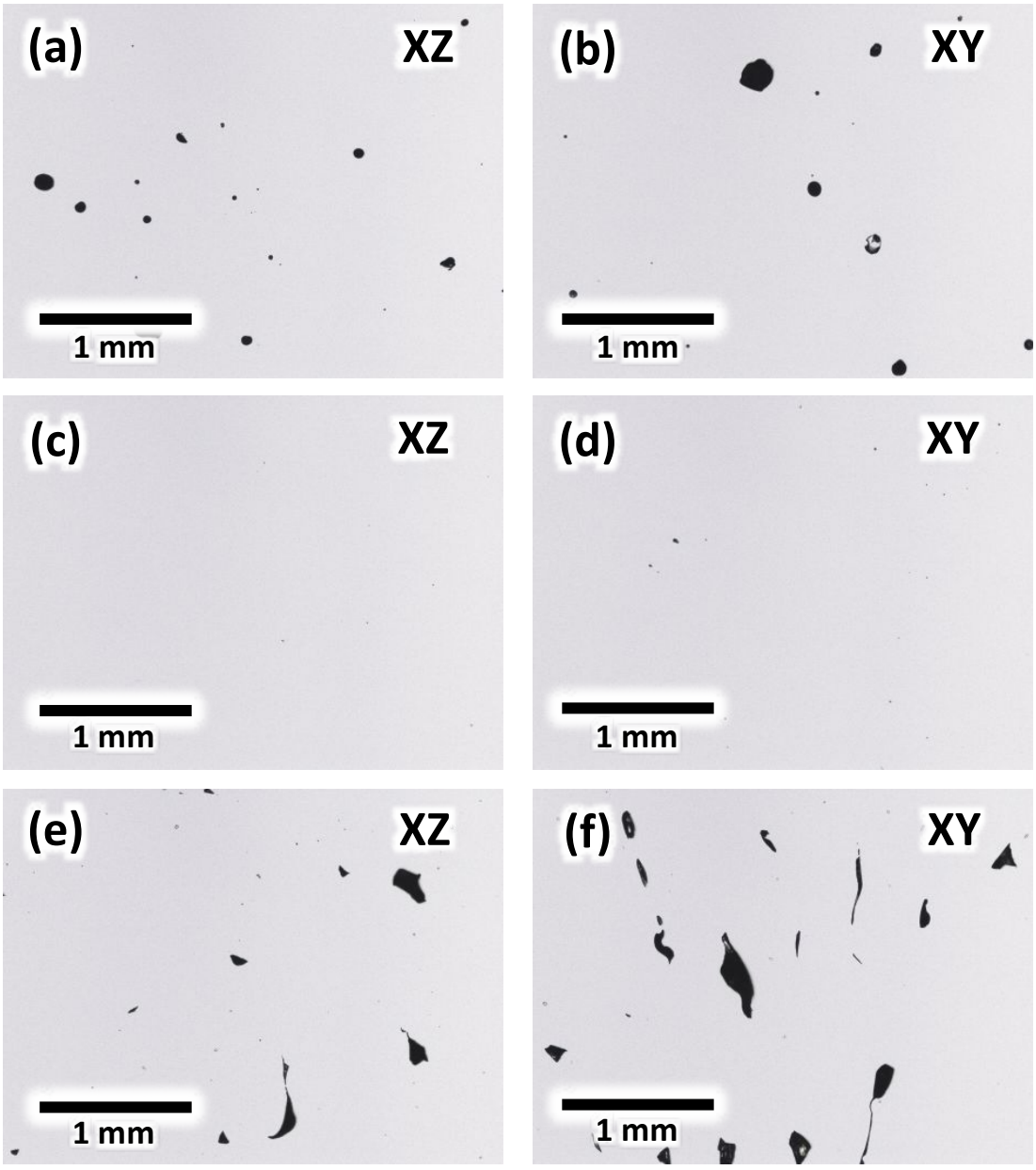


Figure 4: Optical micrographs from IN718 exhibiting (a,b) keyhole pores, (c,d) full density and (e,f) lack of fusion flaws from the (a,c,e) XZ and (b,d,f) XY cross sections. These samples fabricated with varying laser scan speed while power (275 W) hatch spacing (120 µm), and slice thickness (30 µm) were kept constant.


Figure 5: Optical micrographs of XZ and XY cross sections of IN718 samples produced with varying laser power and laser scan speed, while hatch spacing (120 µm), and slice thickness (30 µm) were kept constant.

### *3.3 Effect of laser power and scan speed on relative density*

All metallurgical flaws were quantified on both XY and XZ cross sections, as presented in Figure 6. While the average relative density obtained using Archimedes' method was, in general, lower than that obtained via image analysis, the overall trend as functions of LPBF parameters remained consistent for both methods of measurements. Samples with the highest relative density were found at moderate scan speeds within their respective laser power and scan speed ranges. For all laser powers examined, the relative density gradually increased to a maximum and then gradually decreased as a function of scan speed.

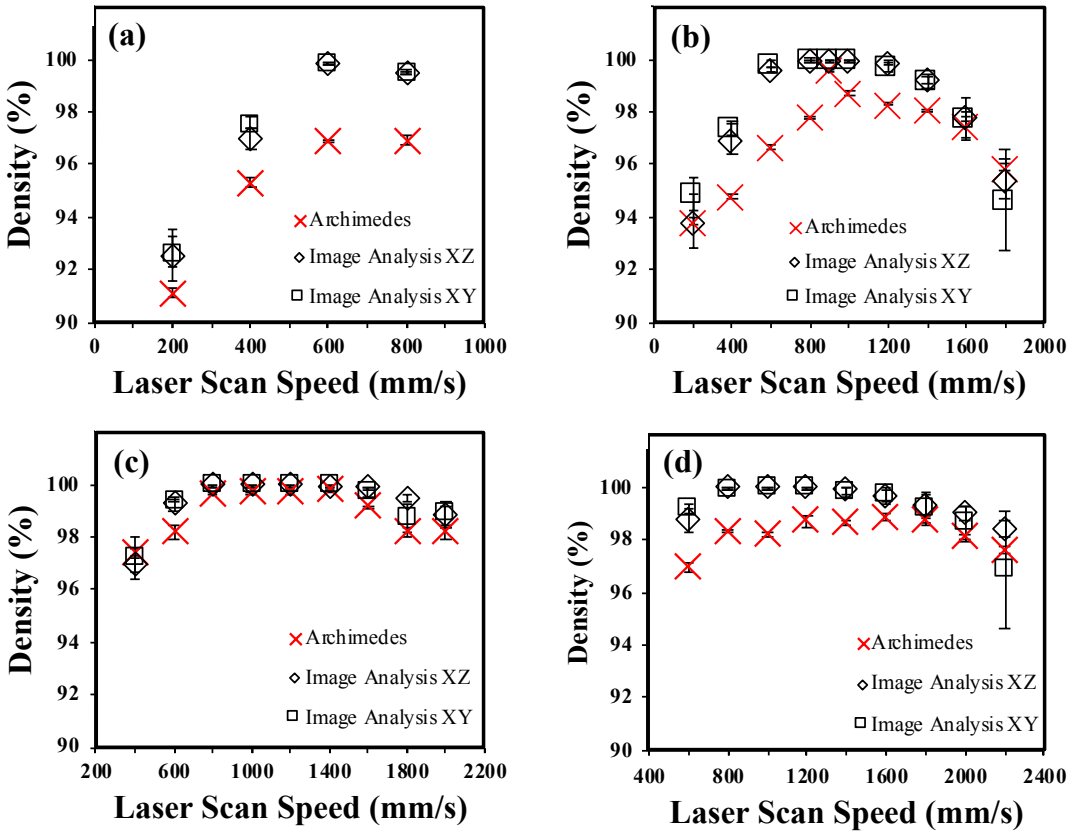


Figure 6: Relative sample density as a function of laser scan speeds at constant hatch spacing and slice thickness of 120 µm and 30 µm, respectively, for laser power of (a) 125 W; (b) 200 W; (c) 275 W; and (d) 350 W.

The relative density was also plotted in Figure 7 as a function of energy density, as determined by Eq. (1). When fused with a laser power of 125 W, the relative density was highest at 57.9 J/mm$^3$ and gradually decreased as energy density increased. This pattern of changing relative density was more clearly observed when fabricated at higher laser powers, e.g., 200 W, 275 W, and 350 W. As illustrated in Figures 7(b), 7(c) and 7(d), the relative density increased sharply before reaching the maximum. The decrease in relative density over an increasing range of energy density appeared to be more gradual at higher laser powers compared to lower laser powers. For all investigated laser powers, the relative density was the highest when energy density employed was between 50 and 100 J/mm$^3$, and this observation is consistent with the literature [42,43].

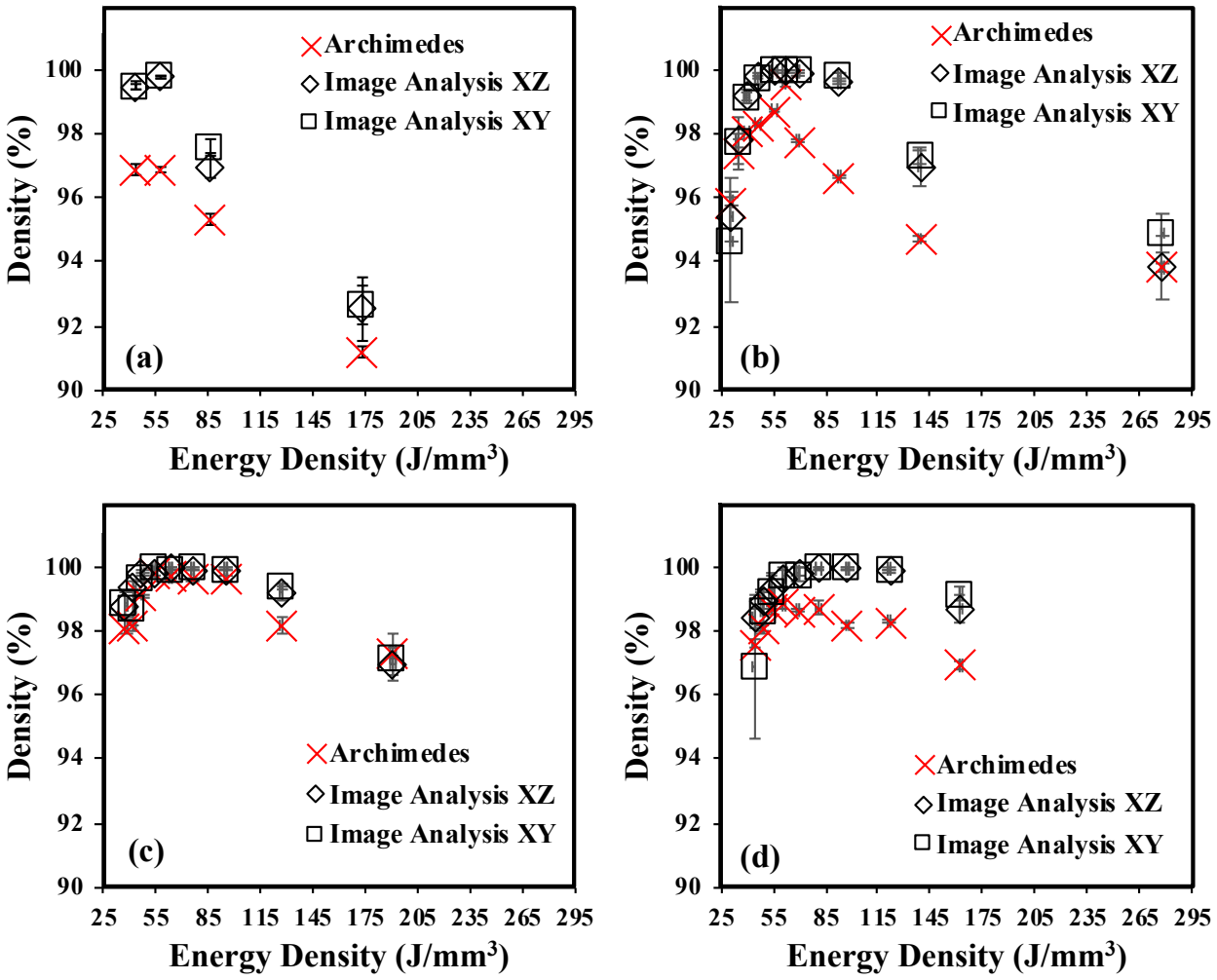


Figure 7: Relative sample density as a function of energy density at hatch spacing, slice thickness, and scan rotation angle of 120 µm, 30 µm, and 16°, respectively, for laser power of (a) 125 W; (b) 200 W; (c) 275 W; and (d) 350 W.

A simplistic model was devised to quantitatively correlate the relative density and volumetric energy density. Assuming thermally activated processes of melting and evaporation, exponential functions were defined by:

$$Relative\ Density = 100 - Aexp(-b * E_\rho^v) - Cexp(d * E_\rho^v - f) \quad (2)$$

where $A$, $b$, $C$, $d$, and $f$ are constants, and $E_\rho^v$ is the volumetric energy density. Constants $A$ and $b$ approximates the density curve at low energy density where fusion is dependent on the melting behavior of the material. $C$, $d$, and $f$ approximate the density curve at high energy density, where keyhole formation related to evaporation would take place. Figure 8(a) plots the sample relative density with respect to the $E_\rho^v$. At first glance, Figure 8(a) demonstrate a good fit. However, Table 3 outlines the calculated constants as defined by Eq. (2), and the corresponding residuals for 5 prediction iterations with nearly constant root-mean-square error (RMSE) at 7.2. While constants $A$, $b$, $d$, and $f$ have relatively low standard deviations, the pre-exponential constant $C$ have a high standard deviation. This indicates some inconsistency between the model and the experimental data. Notice that there are no experimental data below 30.86 J/mm$^3$ and this is strictly due to insufficient energy to melt/fuse the powder bed. As such, the model attempted the fit without any experimental data below 30.86 J/mm$^3$, or a boundary condition corresponding to zero energy density.

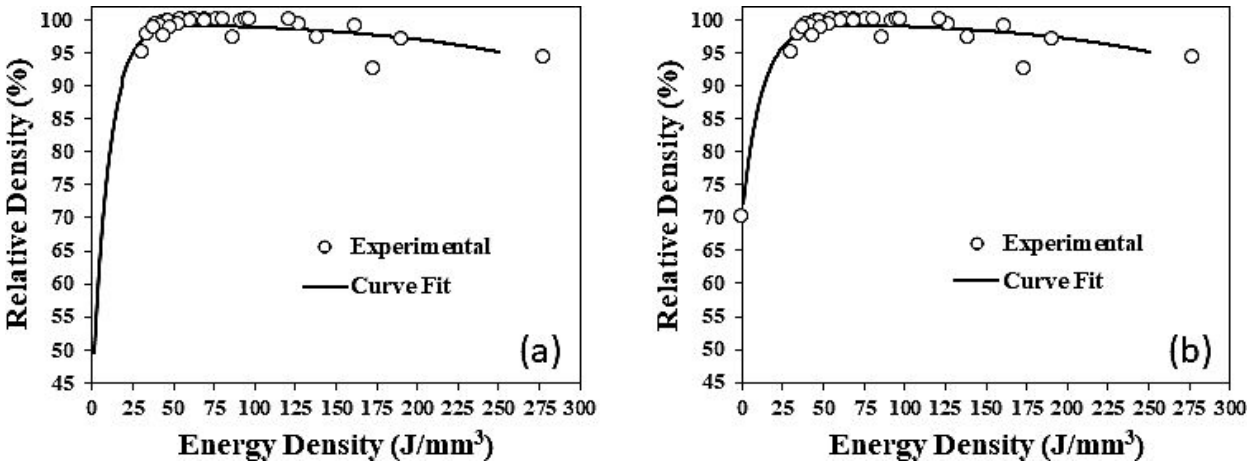


Figure 8: Predicted and experimental relative densities as a function of energy density (a) without and (b) with density (e.g., powder packing) of 70 % corresponding to zero energy density.

Table 3: Calculated constants without artificial relative density point.

| Iteration | *A* | *b* ($mm^3/J$) | *C* | *d* ($mm^3/J$) | *f* | *RMSE* |
|---|---|---|---|---|---|---|
| 1 | 58.24468 | 0.10136 | 10.20256 | 0.00999 | 3.29402 | 7.20753 |
| 2 | 54.37903 | 0.10059 | 11.27128 | 0.01003 | 3.40288 | 7.21968 |
| 3 | 52.08941 | 0.09667 | 19.76539 | 0.01028 | 4.02188 | 7.21910 |
| 4 | 52.36739 | 0.09656 | 18.45234 | 0.01025 | 3.94879 | 7.22158 |
| 5 | 58.94424 | 0.10135 | 21.88401 | 0.01025 | 4.11260 | 7.18741 |
| **Average (StDev)** | 55.20495 (3.22733) | 0.09931 (0.00248) | 16.31511 (5.25092) | 0.01016 (0.00014) | 3.75603 (0.03785) | 7.21106 (0.01433) |

While the perfectly closest packing density of mono-sized spheres or powders cannot be more than $\pi/(3\sqrt{2}) \approx 0.74$ [44], a narrow gaussian distribution of powders should have lower packing density. For a narrow particle radii range between 0.67 – 1.5 of the mean, the packing density and coordination number are ~0.58 and ~5.9 respectively [45]. Since the IN718 powder feedstock particle radii range between ~0.33 – ~1.76 of the mean, the theoretical packing density should be no higher than 70%. As such, an assumed relative density value of 70 % was added at an energy density of zero J/$mm^3$. Figure 8(b) shows the curve fit obtained from the model and the experimental data as a function of energy density. Although similar to Figure 8(a), the additional data point at zero J/$mm^3$ reduced the standard deviation reported in Table 4, including that for the constant *C*. A consistent RMSE was approximately 7.3.

Table 4: Calculated constants with artificial relative density point.

| Iteration | *A* | *b* ($mm^3/J$) | *C* | *d* ($mm^3/J$) | *f* | *RMSE* |
|---|---|---|---|---|---|---|
| 1 | 29.75860 | 0.08421 | 2.22715 | 0.01099 | 1.98692 | 7.32819 |
| 2 | 29.75435 | 0.08434 | 1.56237 | 0.01095 | 1.61892 | 7.32851 |
| 3 | 29.76189 | 0.08409 | 2.40009 | 0.01105 | 2.07363 | 7.32804 |
| 4 | 29.75306 | 0.08442 | 1.71224 | 0.01091 | 1.70366 | 7.32879 |
| 5 | 29.75328 | 0.08429 | 2.05710 | 0.01097 | 1.90092 | 7.32832 |
| **Average (StDev)** | 29.75622 (0.00384) | 0.08427 (0.00013) | 1.99179 (0.34961) | 0.01097 (0.00005) | 1.85679 (0.19098) | 7.32837 (0.00029) |

### *3.4 Effect of laser power and scan speed on microstructure*

Figure 9 depict the typical layer by layer microstructure and the melt pool characteristics of IN718 samples produced at constant laser power of 125 W, and varying laser scan speeds. Both the melt pool width and depth decreased with increasing laser scan speed. Figures 9(a) and 9(b) present the microstructure of samples produced with high energy density, in which deep keyhole melt pools solidified producing spherical keyhole pores. By increasing laser scan speed to 600 mm/s and 800 mm/s, as presented in Figure 7(c) and 7(d), respectively, a clear decrease in porosity was observed. A decrease in melt pool dimensions is reflective of the engagement in conduction mode during laser-material interaction. This trend in decreasing melt pool dimensions as a function of laser scan speed was consistent for all laser powers examined in this study.

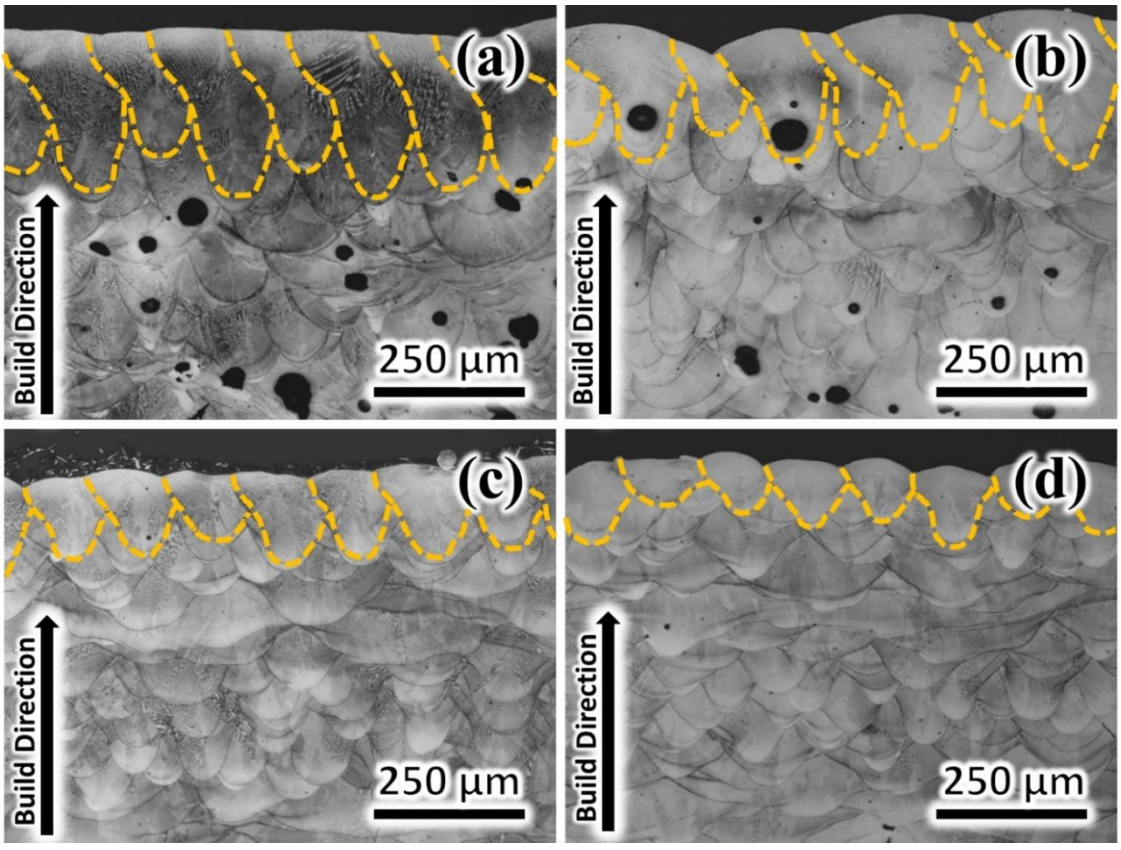


Figure 9: Melt pools observed parallel to the build direction at scan speeds of: (a) 200 mm/s, (b) 400 mm/s, (c) 600 mm/s, (d) 800 mm/s. Laser power, hatch spacing, slice thickness, and scan rotation angle were constant at 125W, 120 µm, 30 µm, and 16°, respectively.

Rosenthal's equation [46] can be employed as a simple analytical expression to estimate the melt pool development over a wide range of laser powers and scan speeds as described below:

$$T = T_o + \frac{Q}{2\pi R k}\exp\left(\frac{-v(\xi + R)}{2\alpha}\right) \quad (2)$$

where $T$ is the final temperature, $T_o$ is the build plate temperature, $P$ is the laser power, $k$ is thermal conductivity [47], $v$ is laser scan speed, $R = (\xi^2+y^2+z^2)^{1/2}$ is the radial distance from the center of the laser beam, $\alpha$ is the thermal diffusivity, $\xi$ is the distance along the beam travel direction, y is the distance parallel to the build plate, and z is the distance parallel to the build direction.

The predicted melt pool dimensions and experimentally measured dimensions are presented in Figure 10. The calculated melt pool width corroborates well to the experimental measurement, and clearly depicts a gradual decrease over an increasing range of laser scan speeds at a constant laser power. However, melt pool depths calculated using Rosenthal's equation underestimated the experimental ones for samples, especially for those fabricated with high energy input, up to 350 %. As the laser scan speed increased, the predicted melt pool depths were more comparable to the experimental results.

At slow scan speeds, i.e., high energy densities, the magnitude of the measured melt pool depth was much higher than the measured melt pool width. This trend was more prevalent for higher laser powers – indicative of keyhole mode. An engagement in conduction mode at higher laser scan speeds beyond the high energy density threshold produced shallower melt pools. Samples fabricated at 125 W exhibited a more gradual decrease in melt pool depth compared to the steep decrease observed with higher laser powers. Since the Rosenthal equation yields the predicted temperature both at and below the interacting surface, combinations of $\xi$, y, and z, in

which the temperature reaches the liquidus temperature will provide estimates of the melt pool size and shape. Thus, unstable keyholes with significant internal temperature variation and dynamic fluid flow [48] need to be incorporated into the model in order to correctly predict the formation of melt pool depth at high energy density [49-54].

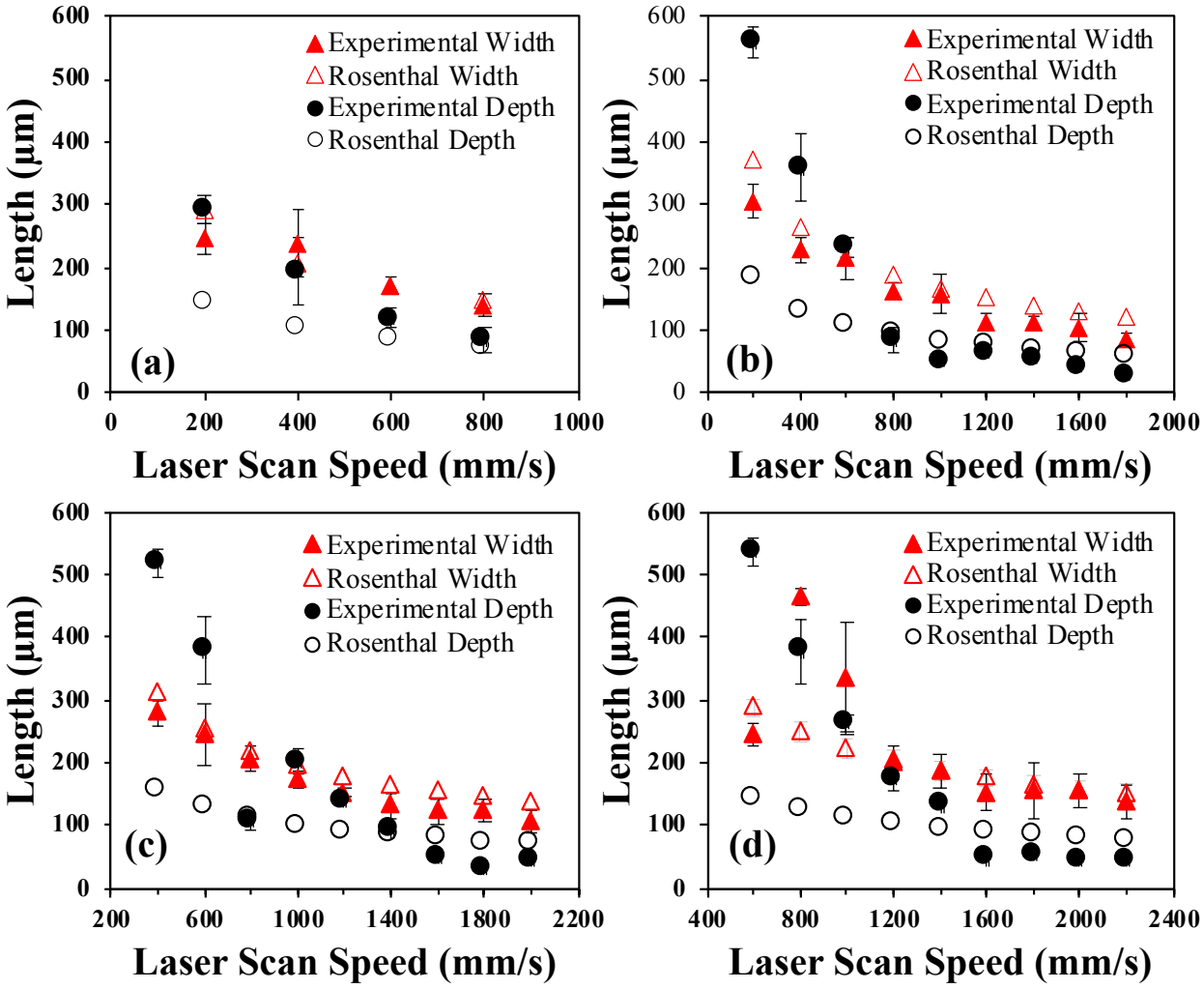


Figure 10: Melt pool dimensions experimentally measured and predicted by Rosenthal's equation as a function of laser scan speed at constant hatch spacing, slice thickness, and scan rotation angle of 120 µm, 30 µm, and 16°, respectively, for laser power of (a) 125 W; (b) 200 W; (c) 275 W; and (d) 350 W.

Figure 11 present typical microstructure of IN718 sample produced by LPBF with overlapping consecutive melt pools generated by the layer-by-layer fusion process. This is common when viewing parallel to the build direction, i.e., XZ cross section as shown in Figure 11(a). Figure 11(b) presents overlapping melt pools as a network of discontinuous and multidirectional laser tracks in the XY cross section based on scan rotation angle. BSE micrograph in Figure 11(c) depicts melt pool boundaries, equiaxed cells and elongated dendritic microstructure in the XZ cross section. The XY cross section shown by the high magnification BSE micrograph, presented in Figure 11(d), revealed a more equiaxed cellular network.

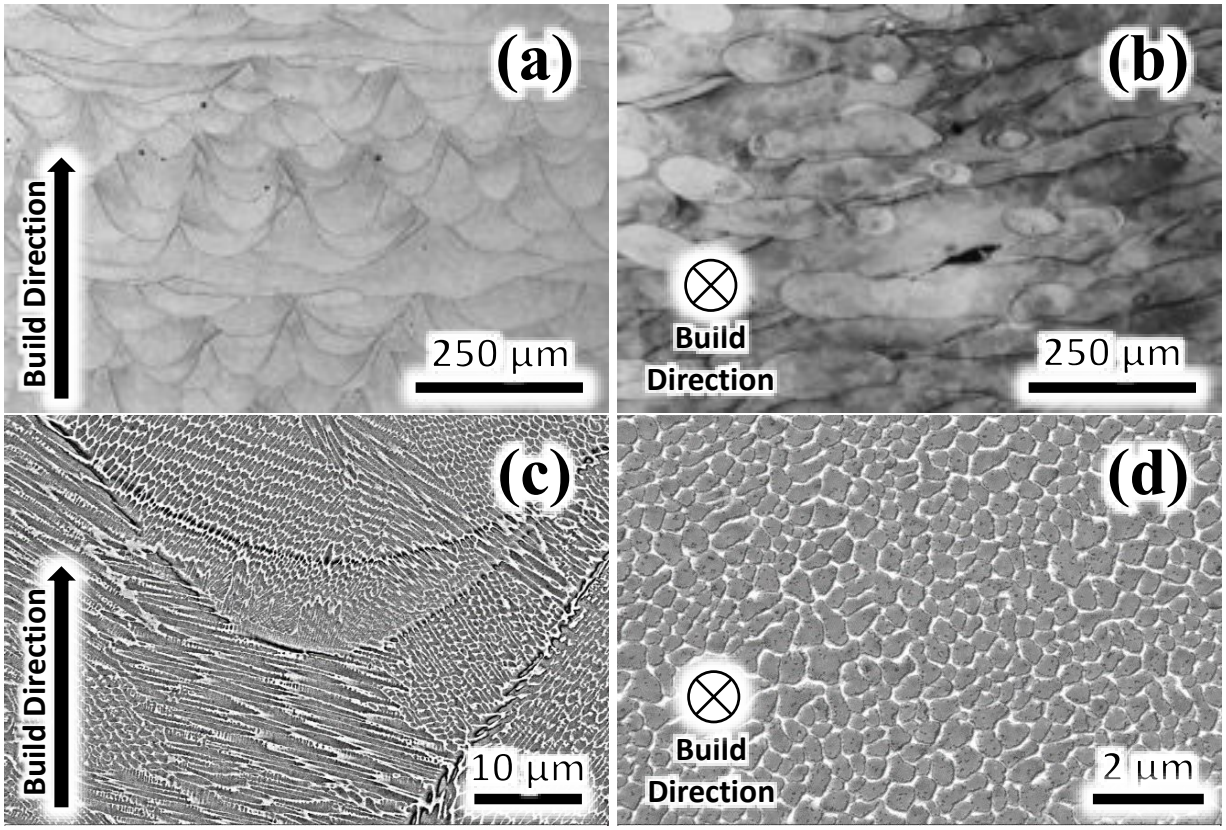


Figure 11: Optical micrographs of SLMed IN718 obtained (a) parallel to the build direction and (b) perpendicular to the build direction. Backscatter electron micrographs of SLMed IN718 (c) parallel to the build direction and (b) perpendicular to the build direction. Laser power, laser scan speed, hatch spacing, slice thickness, and scan rotation angle were constant at 125 W, 800 mm/s, 120 µm, 30 µm, and 16°, respectively.

Due to the invariability and equiaxed cellular network found in the XY cross sections, quantification of the cell size was conducted only using micrographs taken from the XY plane. Figure 12 illustrate the change in the average cell size as a function of laser scan speeds at different laser powers. As scan speed increased, the average cell size decreased. In other words, reduction in energy density corresponds to the reduction in average cell size, and this trend was consistent for all laser powers investigated in this study.

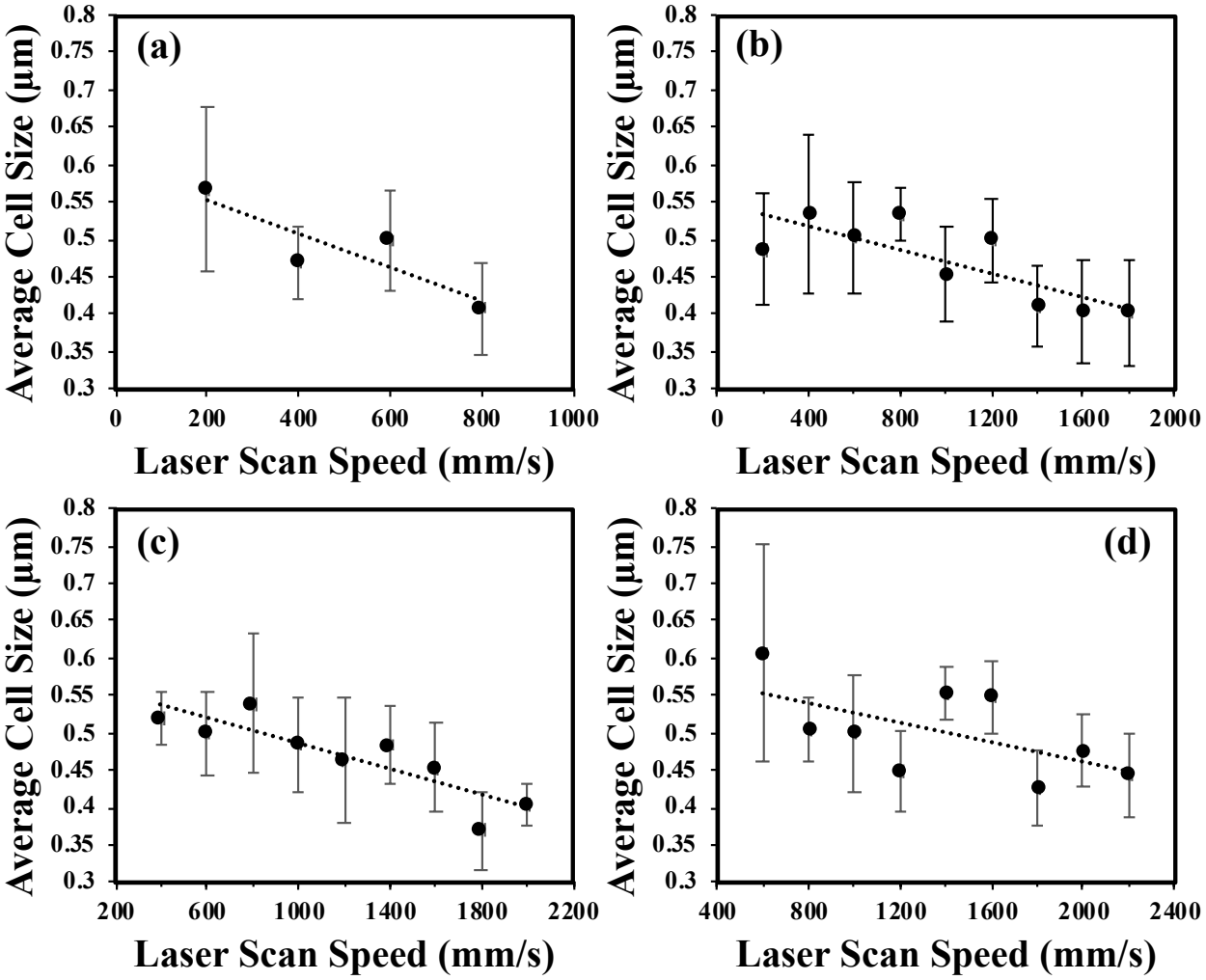


Figure 12: Variation in average cell size as a function of laser scan speed. Laser power, hatch spacing, slice thickness, and scan rotation angle were held constant at 125 W, 120 µm, 30 µm, and 16°, respectively, for laser power of (a) 125 W; (b) 200 W; (c) 275 W; and (d) 350 W.

The cooling rate can be correlated to the measured cell size. A phenomenological method that relates the secondary dendrite arm spacing (SDAS) to the cooling rate was employed, in which the measured cellular spacing was used in leu of the SDAS. The cooling rate was approximated using the following expression [55]:

$$\lambda = \mathrm{m}\dot{T}^{-\mathrm{n}} \tag{3}$$

where $\lambda$ is the cellular spacing, $\dot{T}$ is the cooling rate, m and n are materials constants, equal to 50 and 0.33, respectively, for IN718 [56].

In addition, Rosenthal's equation describes the change in temperature of a moving point heat source, which can be employed to estimate the change in temperature of a moving laser at a specified laser scan speed. Thus, the cooling rate, $\dot{T}$ of each sample was also estimated using Rosenthal's equation to illustrate the trend of cooling rates as a function of laser scan speeds. A simplified Rosenthal solution [57] used to determine the cooling rates is expressed by:

$$\dot{T} = 2\pi k(T_s - T_o)(T_L - T_o)\frac{v}{PA} \tag{4}$$

where $k$ is the thermal conductivity, $T_s$ is the solidus temperature, $T_o$ is the build plate temperature, $T_L$ is the liquidus temperature, $v$ is the laser scan speed, $P$ is the laser power, and $A$ is the laser absorption coefficient. Eq. (4) assumes constant average thermal properties such as thermal conductivity and laser absorptivity; however, this is not the case in LPBF. Based on highspeed imaging [11], the powder bed melts within a few microseconds; therefore, calculations were carried out using materials constants at both the room temperature and the liquidus temperature to distinguish the difference in the trend of the cooling rates. The thermal conductivity of IN718 used in Eq. (4) at room temperature and liquidus temperature are 11.4 W/m·K and 26.7 W/m·K,

respectively [47,58]. The laser absorptivity of IN718 at room temperature and liquidus temperature are 0.62 and 0.07, respectively [49].

Figure 12 presents cooling rates estimated by using thermal properties of IN718 at the liquidus temperature, i.e., Rosenthal (liquid) and at room temperature, i.e., Rosenthal (solid). The measured cellular spacing assumed as SDAS yielded cooling rates in the range of $10^6$ K/s for all processing parameters examined. Cooling rates estimated based on Rosenthal's equation using room temperature thermal properties was in the order of $10^5$ K/s to $10^6$ K/s. The cooling rates calculated using Rosenthal's equation with thermal conductivity and laser absorptivity of the liquid phase yielded cooling rates in the order of $10^6$ to $10^7$ K/s. In general, the estimated cooling rates increased as the laser scan speed increased, which corroborated well to the decreasing cell size observed with faster laser scan speeds as seen in Figure 11. Moreover, the cooling rate determined from the measured cell size lied between the estimate by Rosenthal's equation with liquidus and solid (room temperature) properties.

The SDAS is an important characteristic in solidification microstructure because it is related to the diffusion distance in the solidification process and directly influences the microsegregation. The simple model proposed by Kattamis *et* al. [55] was used to predict the final SDAS based on coarsening mechanism. Since the cell size was used in place of the secondary dendrite arm, the approximated cooling rate can only provide a semiempirical relationship between the cooling rate and the laser scan speed at constant power. Nonetheless, the estimated values obtained from Eq. (3) are quite consistent with numerically simulated values for the SLM process [59]. Although the estimated cooling rates from the Rosenthal equation used constant thermophysical properties of IN718 at the liquidus or room temperature, the trend and magnitude were comparable to those estimated from the measurement of cell size. Since the use of Eq. (4)

rely on thermophysical constants, estimated values can only illustrate the trend of cooling rates over a range of laser scan speed.

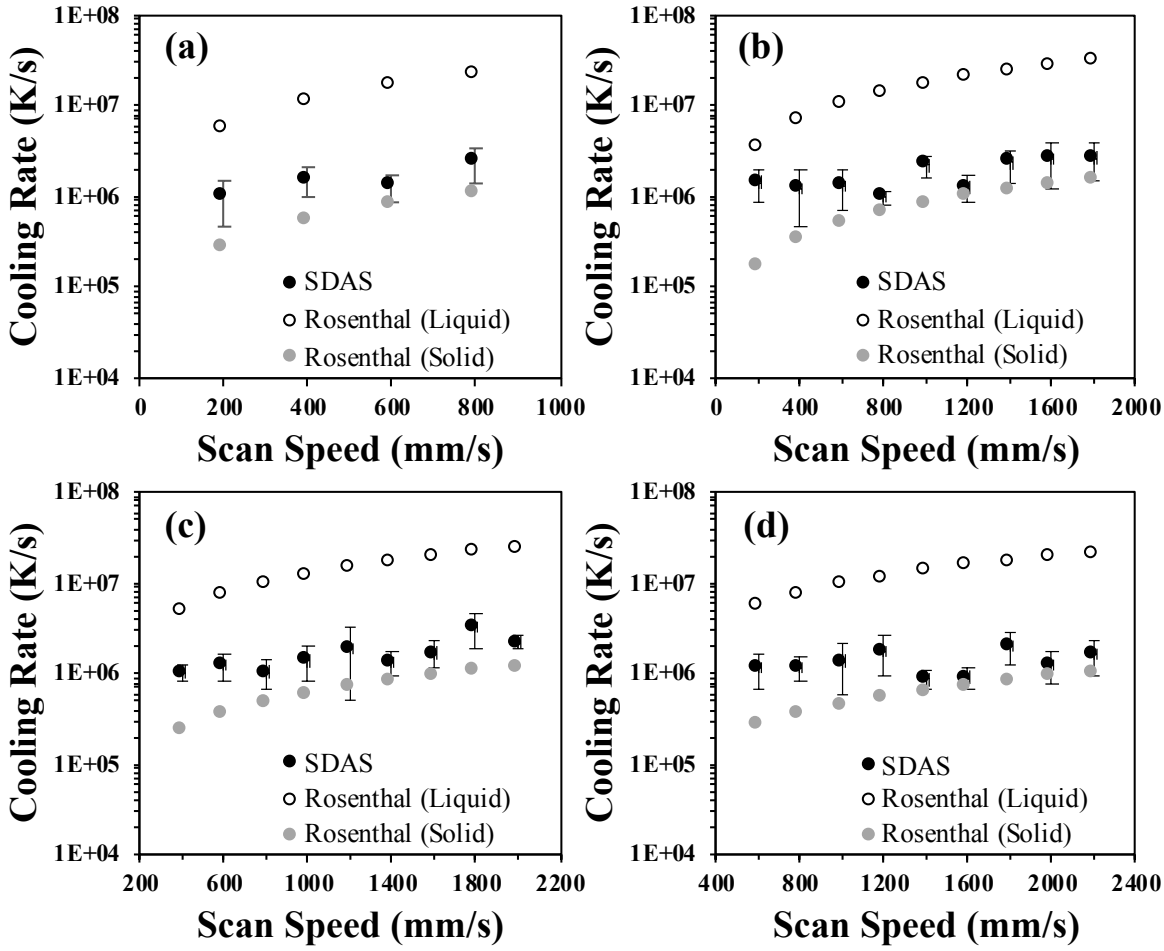


Figure 13: Comparison between SDAS and Rosenthal cooling rates at varying laser powers and scan speeds at constant hatch spacing, slice thickness, and scan rotation angle of 120 µm, 30 µm, and 16°, respectively, for laser power of (a) 125 W; (b) 200 W; (c) 275 W; and (d) 350 W.

### *3.5 Effect of laser scan rotation angle*

To examine the influence of laser scan rotation angle on the relative density: laser scan speed, hatch spacing, and slice thickness were kept constant at 900 mm/s, 120 µm, 30 µm, respectively. As depicted in Figure 14, when fused with 200 W or higher, the variation in laser scan rotation angle had minimal influence on the overall part density. However, samples fused

with 125 W had significant differences in defect formation. The unidirectional scanning (0 degrees) produced a semi-continuous pattern of flaws across the XZ and XY cross sections. At an angle rotation of 16 degrees, the semi-continuous network of defects was replaced by sparsely distributed flaws. At scan rotation angles of 30, 45, and 60 degrees, some amounts of networked flaws were observed. Increasing the scan rotation angle to 90 degrees produced a grid-like pattern of flaws from alternating layers of laser tracks.

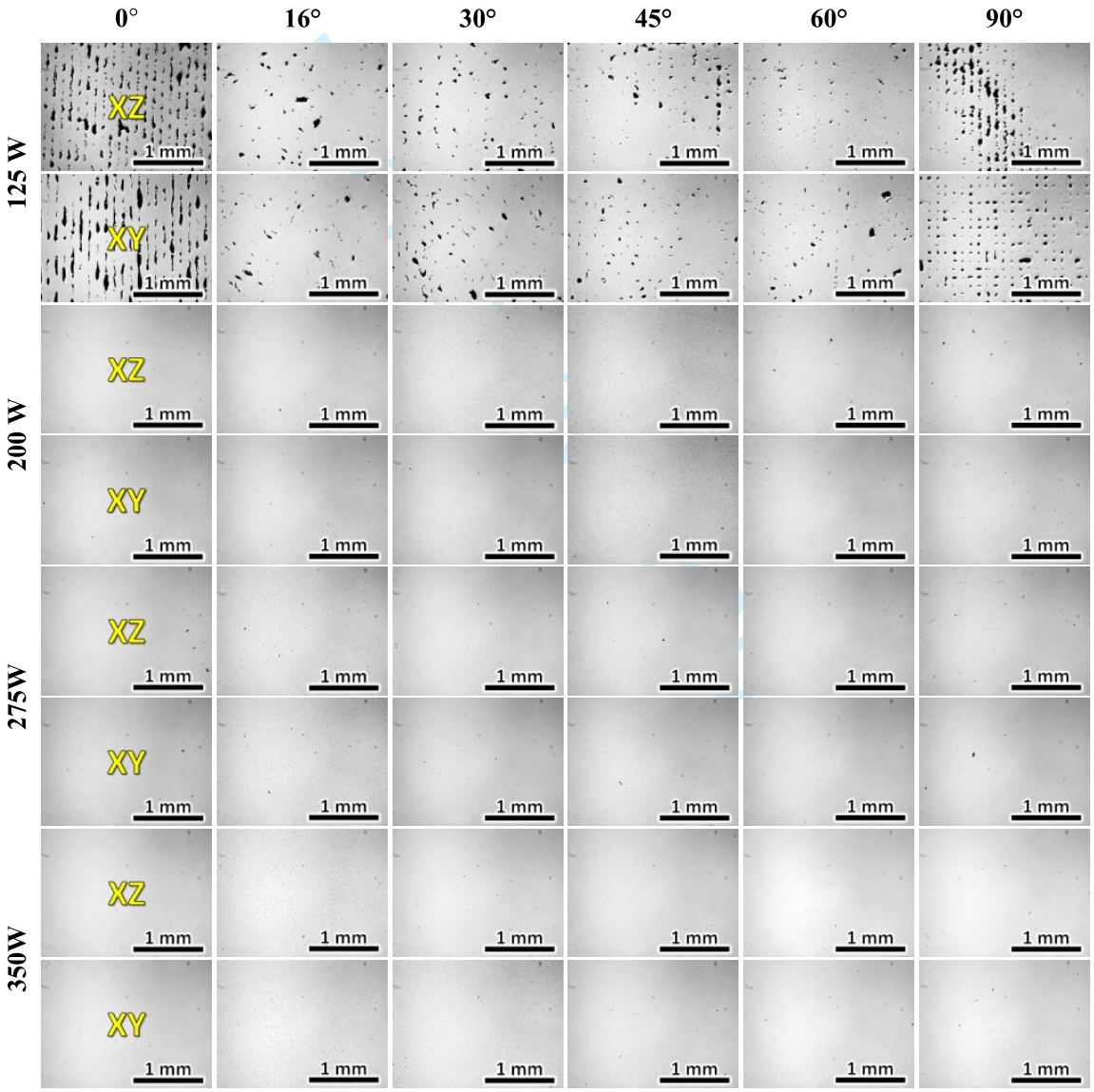


Figure 14: Optical micrographs from IN718 samples produced as functions of laser power and scan rotation angle. The other parameters, laser scan speed, hatch spacing, and slice thickness were kept constant at 900 mm/s, 120 µm, 30 µm, respectively.

Figure 15 plots the relative density of IN718 samples as a function of laser scan rotation angles for various laser powers. The relative density of specimens fabricated at 125 W using scan rotation strategies of 0° and 90° resulted in low relative densities of ~90% and ~96%, respectively. In contrast, the relative densities of samples fabricated at 16°, 30°, 45°, and 60° using 125 W were nearly identical. In general, higher laser powers of 200 W, 275 W and 350 W produced dense samples regardless of scan rotation angle.

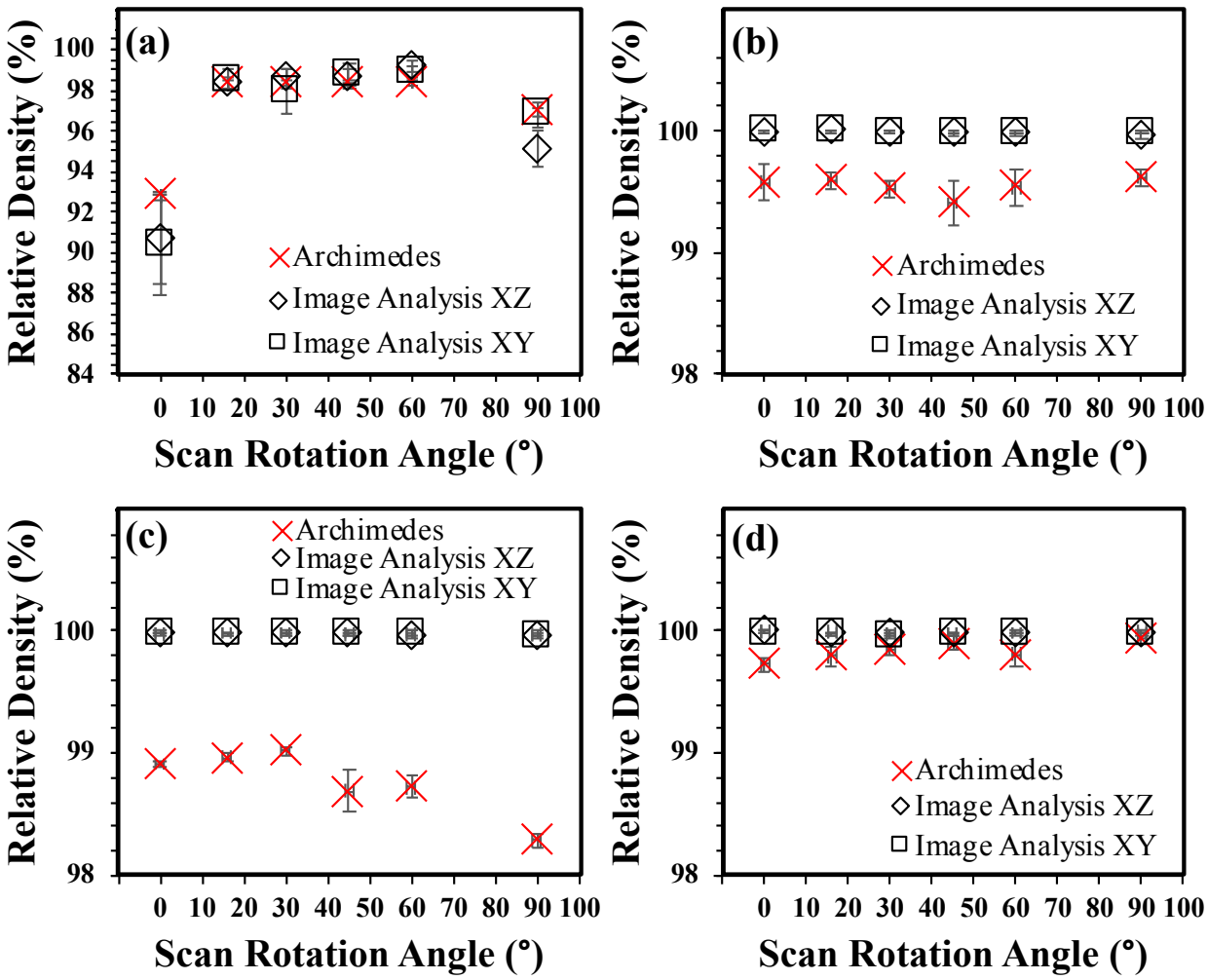


Figure 15: Relative density as a function of laser scan rotation angles at laser power of (a) 125 W; (b) 200 W; (c) 275 W; and (d) 350 W. Scan speed, hatch spacing, and slice thickness were held constant at 900 mm/s, 120 µm, and 30 µm, respectively.

Quantification of melt pool dimensions were also obtained for the samples printed as a function of laser scan rotation angle as presented in Figure 16. No discernable trend in melt pool width and depth was observed as a function of scan rotation angle regardless of laser power employed. Overall, the melt pool widths were larger than the depths, which corresponds to conduction melting mode.

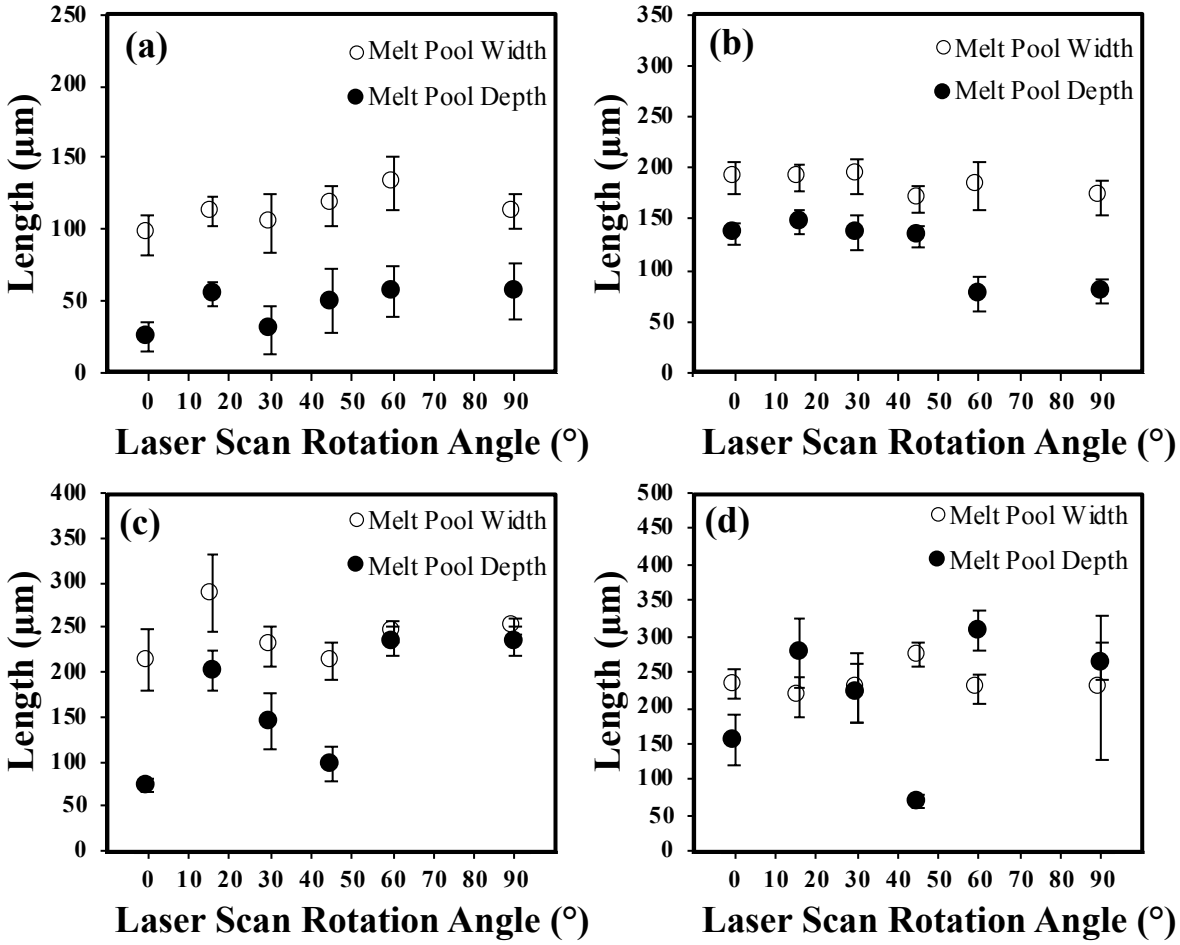


Figure 16: Melt pool dimensions as a function of laser scan rotation angles at laser power of (a) 125 W; (b) 200 W; (c) 275 W; and (d) 350 W. Scan speed, hatch spacing, and slice thickness were held constant at 900 mm/s, 120 µm, and 30 µm, respectively.

Figure 17 presents the BSE micrographs of equiaxed cellular structures observed perpendicular to the build direction. The equiaxed cellular microstructure in IN718 were produced regardless of laser scan rotation angle and laser power. Figure 18 presents the measured cell size

as a function of laser scan rotation angle at each laser power. Using laser power of 125 W and 250 W, the variation in laser scan rotation angles had minimal effect on the average cell size; except at 125W, the average cell size of sample printed using laser scan rotation of 0 degrees were noticeably larger than those from other scan rotation angles. This phenomenon is most likely due to the poor heat dissipation within the sample during solidification.

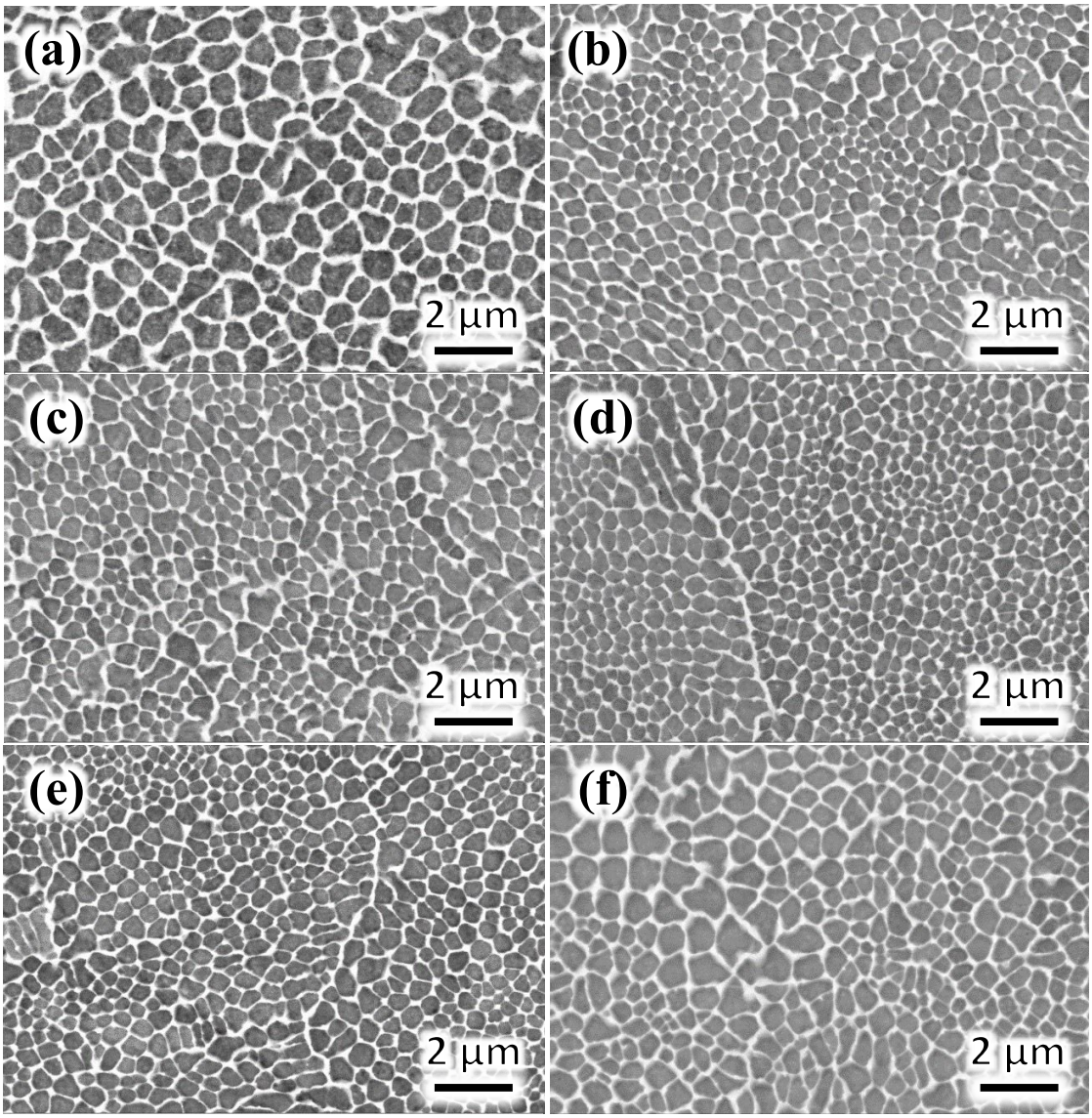


Figure 17: BSE micrographs showing cellular microstructure observed perpendicular to the build direction as a function of laser scan rotation angle of (a) 0°, (b) 16°, (c) 30°, (d) 45°, (e) 60°, and (f) 90°. Laser power, scan speed, hatch spacing, and slice thickness were held constant at 125 W, 900 mm/s, 120 μm, and 30 μm, respectively.

To highlight the potential influence of melt pool development and its influence on heat dissipation, i.e., conduction paths, Figure 19 compares the difference in melt pool development between samples fabricated at constant power, speed, scan rotation and slice thickness, but using different hatch spacings. Figure 19(a) shows the XZ cross section of the sample without laser scan rotation strategy. Lack of fusion flaws were observed between each laser raster, separated by 120 µm. The inherent voids and free space, such as those shown in Figure 14 for the laser power of 125 W, would prevent effective conductive heat transfer during the LPBF.

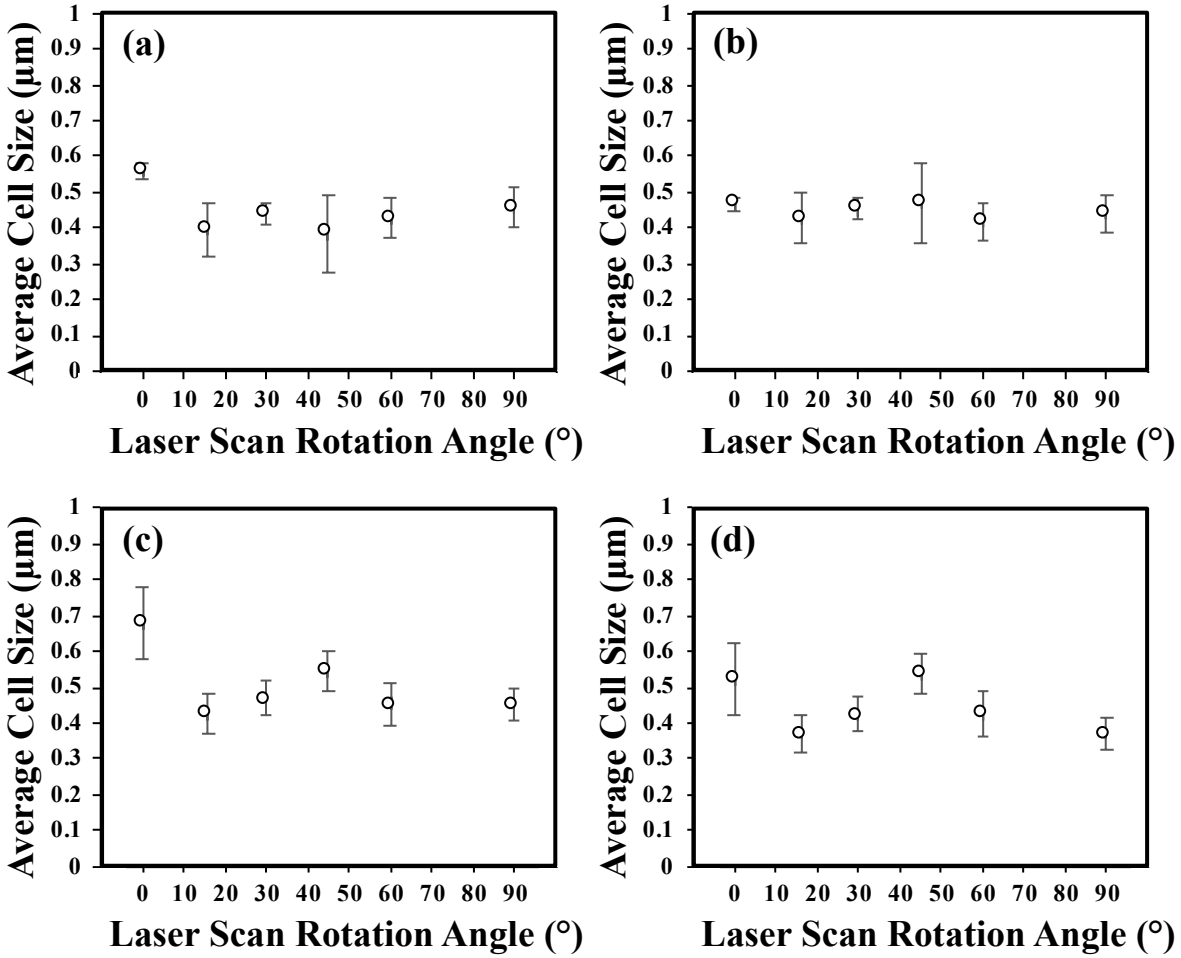


Figure 18: Average cell size as a function of laser scan rotation angles at laser power of (a) 125 W; (b) 200 W; (c) 275 W; and (d) 350 W. Scan speed, hatch spacing, and slice thickness were held constant at 900 mm/s, 120 µm, and 30 µm, respectively.

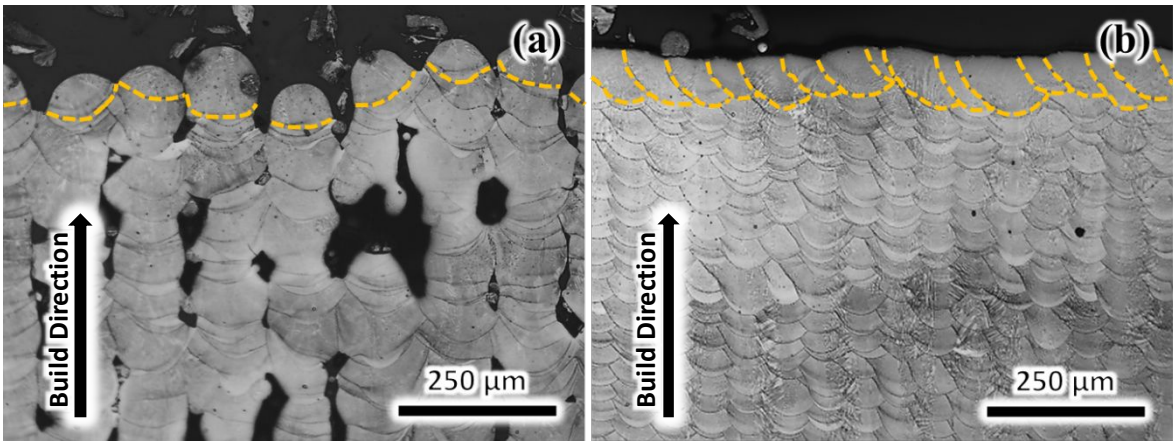


Figure 19: Optical micrographs of XZ cross section with laser power, scan speed, and slice thickness of 125 W, 900 mm/s, 30 µm, respectively, at hatch spacing: (a) 120 µm, (b) 60 µm.

Figure 18(c) and 18(d) plots the average cell size as a function of laser scan rotation angles at higher laser powers of 275 W and 350 W. The average cell size seemed to vary more as a function of laser scan rotation angles. The relationship between cell size and laser scan speed plotted in Figure 12 demonstrated that the average cell size can be related to the cooling rate of the melt pool as reported in Figure 13. Through single laser track studies, Wang *et* al. [32] compared the solidification behavior between melt pools under conduction and keyhole mode. They observed that the thermal gradient, $G$ and solidification rate, $R$ varied within the melt pool. From the bottom to the top, $G$ decreased, and $R$ increased, regardless of melting modes. While the cooling rate, $\dot{T}$ can be related to the cell size in Eq. (3), $\dot{T}$ can be further related to $G$ and $R$ in the following relation:

$$\dot{T} = GR \text{ [60]} \tag{5}$$

Since the scan speed, hatch spacing, and slice thickness were held constant, the energy density is much greater for the samples fabricated at higher laser powers. The higher energy density will produce deeper melt pools, and thus more variation in $G$ and $R$. Figures 20(a) and 20(b) compare the melt pool depth of specimens fabricated at 200 W and 350 W, respectively. With the

same scan rotation strategy, the sample with the higher energy density have deeper melt pools. High magnification BSE micrographs in Figures 20(c) through 20(e) depict the top, middle, and bottom portions, respectively, of the keyhole melt pool shown in Figure 20(b). These micrographs demonstrate that the cell size can vary at each location within each melt pool. The cell size will vary more, deeper the melt pools, and the variation in cell size at higher laser powers was influenced by the energy density rather than the scan rotation strategy.

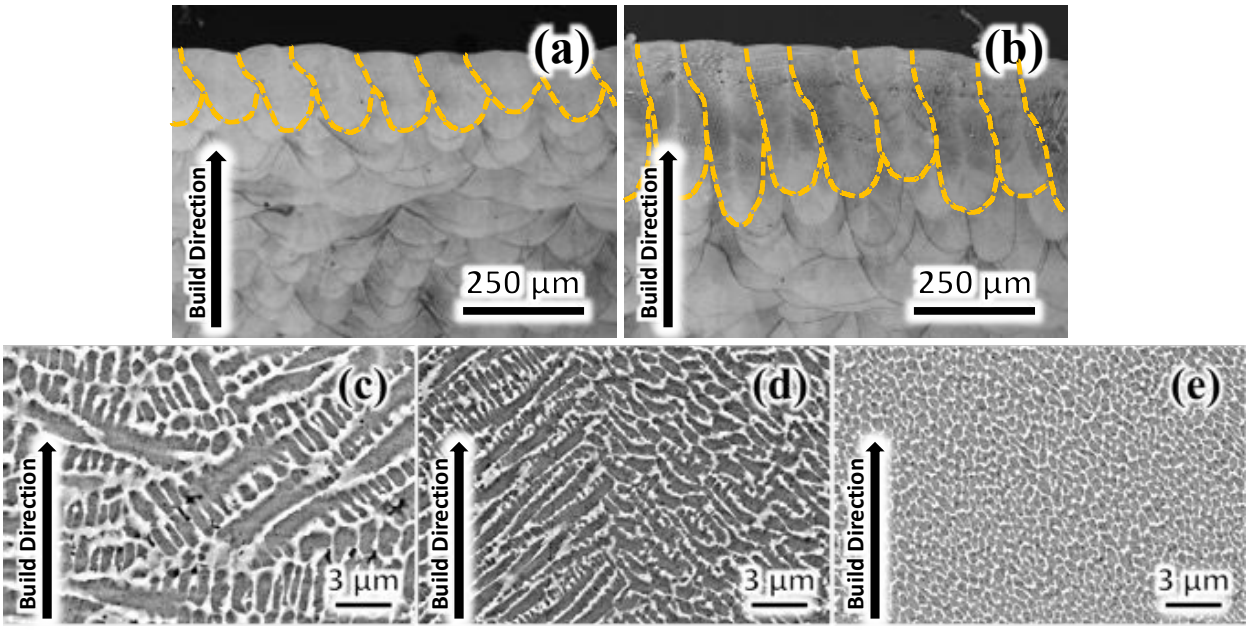


Figure 20: Melt pool comparison between (a) 200 W and (b) 350 W at scan rotation angle, scan speed, hatch spacing, and slice thickness of 16°, 900 mm/s, 120 µm, and 30 µm, respectively. The cell size within deep melt pools observed in (b): (c) near melt pool surface, (d) middle of melt pool, (e) near the bottom of melt pool.

## 4. Concluding Remarks

Effect of LPBF parameters such as laser power, laser scan speed, and laser scan rotation angle, was systematically investigated to examine the solidification microstructure development IN718. Optimal processing windows were observed for all laser powers examined in this study. At low laser power e.g., 125 W, the optimal processing window was small and a more abrupt transition from circular pores to irregular flaws was observed. At higher laser powers, optimal

processing window was enlarged, and the transition from circular porosity to irregular flaws were more gradual. In general, the laser scan rotation strategy had minimal influence on the relative density and the cell size, except at 125 W.

Relative density higher than 99.5% was observed when samples were fabricated with energy density within the range of 50 and 100 J/mm$^3$. The laser-material interaction at low laser scan speeds produced keyhole melt pools with depths much greater than the half width. At moderate laser scan speeds, the optimal processing zone, melt pools had a mixed combination of keyhole and conduction melting. At high laser scan speeds, development of conduction melt pools was observed. Estimated melt pool width by Rosenthal's equation corroborated well to measured melt pool width, however, the melt pool depth estimation underestimated the experimental results, particularly when the energy density was high and keyhole mode was prevalent. A simple empirical model was employed to correlate relative sample density and LPBF volumetric energy density with an assumption of two thermally activated processes, i.e., melting and evaporation. Quantification of the cellular microstructure indicated that there is a decrease in the cellular spacing as the laser scan speed increased at constant power. The cooling rates increased with an increase in laser scan speed. Cooling rates estimated by both the cell size measurement and Rosenthal's equation was in the order of $10^5$ to $10^7$ K/s.

**Acknowledgements**

This research was sponsored by the Battelle Energy Alliances, LLC under a contract, No. DE-AC07-05ID14517-214376 with collaboration from authors of Idaho National Laboratory. The views, opinions and conclusions made in this document are those of the authors and should not be interpreted as representing the official policies, either expressed or implied, of the Battelle Energy Alliances or Idaho National Laboratory or the U.S. Government. The U.S. Government is

## References


1. W.E. King, A.T. Anderson, R.M. Ferencz, N.E. Hodge, C. Kamath, S.A. Khairallah, A.M. Rubenchik, Laser powder bed fusion additive manufacturing of metals; physics, computational, and materials challenges, *Applied Physics Reviews*, **2**(4), 041304 (2015)
2. D. Herzog, V. Seyda, E. Wycisk, C. Emmelmann, Additive manufacturing of metals, *Acta Materialia*, **117**, 371-392 (2016)
3. M. Lewandowski, V. Sahai, R. Wilcox, C. Matlock, R. Overfelt, High temperature deformation of Inconel 718 castings, *Superalloys*, **718**, 625-706 (1994)
4. T.M. Pollock, S. Tin, Nickel-Based Superalloys for Advanced Turbine Engines: Chemistry, Microstructure and Properties, *Journal of Propulsion and Power*, **22**(2), 361-374 (2006)
5. W.E. Frazier, Metal Additive Manufacturing: A Review, *Journal of Materials Engineering and Performance*, **23**(6), 1917-1928 (2014)
6. H. Hyer, L. Zhou, Q. Liu, D. Wu, S. Song, Y. Bai, B. McWilliams, K. Cho, Y. Sohn, High strength WE43 microlattice structures additively manufactured by laser powder bed fusion, *Materialia*, **16**, 101067 (2021)
7. B. Zheng, Y. Zhou, J.E. Smugeresky, J.M. Schoenung, E.J. Lavernia, Thermal Behavior and Microstructure Evolution during Laser Deposition with Laser-Engineered Net Shaping: Part II. Experimental Investigation and Discussion, *Metallurgical and Materials Transactions A*, **39**(9), 2237-2245 (2008)
8. X. Wang, L.N. Carter, B. Pang, M.M. Attallah, M.H. Loretto, Microstructure and yield strength of SLM-fabricated CM247LC Ni-Superalloy, *Acta Materialia*, **128**, 87-95 (2017)
9. H. Hyer, L. Zhou, A. Mehta, Y. Sohn, Effects of alloy composition and solid-state diffusion kinetics on powder bed fusion cracking susceptibility, *Journal of Phase Equilibria and Diffusion*, **42**(1), 5-13 (2021)
10. S. Dadbakhsh, B. Vrancken, J.P. Kruth, J. Luyten, J. Van Humbeeck, Texture and anisotropy in selective laser melting of NiTi alloy, *Materials Science and Engineering: A*, **650**, 225-232 (2016)
11. U. Scipioni Bertoli, G. Guss, S. Wu, M.J. Matthews, J.M. Schoenung, In-situ characterization of laser-powder interaction and cooling rates through high-speed imaging of powder bed fusion additive manufacturing, *Materials & Design*, **135**, 385-396 (2017)
12. R. Konečná, G. Nicoletto, L. Kunz, A. Bača, Microstructure and directional fatigue behavior of Inconel 718 produced by selective laser melting, *Procedia Structural Integrity*, **2**, 2381-2388 (2016)
13. H. Hyer, L. Zhou, S. Park, T. Huynh, A. Mehta, S. Thapliyal, R.S. Mishra, Y. Sohn, Elimination of extraordinarily high cracking susceptibility of aluminum alloy fabricated by laser powder bed fusion, *Journal of Materials Science & Technology*, **103**, 50-58 (2022)
14. L. Zhou, H. Hyer, J. Chang, A. Mehta, T. Huynh, Y. Yang, Y. Sohn, Microstructure, mechanical performance, and corrosion behavior of additively manufactured aluminum alloy 5083 with 0.7 and 1.0 wt% Zr addition, *Materials Science and Engineering: A*, **823**, 141679 (2021)

15. A. Mehta, L. Zhou, T. Huynh, S. Park, H. Hyer, S. Song, Y. Bai, D.D. Imholte, N.E. Woolstenhulme, D.M. Wachs, Y. Sohn, Additive manufacturing and mechanical properties of the dense and crack free Zr-modified aluminum alloy 6061 fabricated by the laser-powder bed fusion, *Additive Manufacturing*, **41**, 101966 (2021)
16. H. Hyer, R. Newell, D. Matejczyk, S. Hsie, M. Anthony, L. Zhou, C. Kammerer, Y. Sohn, Microstructural Development in As Built and Heat Treated IN625 Component Additively Manufactured by Laser Powder Bed Fusion, *Journal of Phase Equilibria and Diffusion*, **42**(1), 14-27 (2021)
17. R. Seede, B. Zhang, A. Whitt, S. Picak, S. Gibbons, P. Flater, A. Elwany, R. Arroyave, I. Karaman, Effect of Heat Treatments on the Microstructure and Mechanical Properties of an Ultra-High Strength Martensitic Steel Fabricated via Laser Powder Bed Fusion Additive Manufacturing, *Additive Manufacturing*, 102255 (2021)
18. A. Mahmud, T. Huynh, L. Zhou, H. Hyer, A. Mehta, D.D. Imholte, N.E. Woolstenhulme, D.M. Wachs, Y. Sohn, Mechanical Behavior Assessment of Ti-6Al-4V ELI Alloy Produced by Laser Powder Bed Fusion, *Metals*, **11**(11), 1671 (2021)
19. L. Zhou, T. Huynh, S. Park, H. Hyer, A. Mehta, S. Song, Y. Bai, B. McWilliams, K. Cho, Y. Sohn, Laser powder bed fusion of Al–10 wt% Ce alloys: microstructure and tensile property, *Journal of Materials Science*, **55**(29), 14611-14625 (2020)
20. S. Kou, A criterion for cracking during solidification, *Acta Materialia*, **88**, 366-374 (2015)
21. S. Kou, Solidification and liquation cracking issues in welding, *JOM*, **55**(6), 37-42 (2003)
22. M.C. Flemings, Solidification processing, *Metallurgical and Materials Transactions B*, **5**(10), 2121-2134 (1974)
23. R.J. Vikram, A. Singh, S. Suwas, Effect of heat treatment on the modification of microstructure of selective laser melted (SLM) IN718 and its consequences on mechanical behavior, *Journal of Materials Research*, **35**(15), 1949-1962 (2020)
24. J. Lee, M. Lee, Correlation Between Microstructure and Tensile Properties of STS 316L and Inconel 718 Fabricated by Selective Laser Melting (SLM), *Journal of Nanoscience and Nanotechnology*, **20**, 6807 - 6814 (2020)
25. E. Chlebus, K. Gruber, B. Kuźnicka, J. Kurzac, T. Kurzynowski, Effect of heat treatment on the microstructure and mechanical properties of Inconel 718 processed by selective laser melting, *Materials Science and Engineering: A*, **639**, 647-655 (2015)
26. X. Wang, P.W. Liu, Y. Ji, Y. Liu, M.H. Horstemeyer, L. Chen, Investigation on microsegregation of IN718 alloy during additive manufacturing via integrated phase-field and finite-element modeling, *Journal of Materials Engineering and Performance*, **28**(2), 657-665 (2019)
27. L. Zhou, A. Mehta, B. McWilliams, K. Cho, Y. Sohn, Microstructure, precipitates and mechanical properties of powder bed fused inconel 718 before and after heat treatment, *Journal of Materials Science & Technology*, **35**(6), 1153-1164 (2019)
28. J.J. Schirra, R.H. Caless, R.W. Hatala, The effect of the Laves phase on the mechanical properties of wrought and cast + HIP Inconel 718, *The Minerals, Metals & Materials Society*, 375 - 388
29. S.A. Mantri, S. Dasari, A. Sharma, T. Alam, M.V. Pantawane, M. Pole, S. Sharma, N.B. Dahotre, R. Banerjee, S. Banerjee, Effect of micro-segregation of alloying elements on the precipitation behaviour in laser surface engineered Alloy 718, *Acta Materialia*, **210**, 116844 (2021)

30. D. Zhang, P. Zhang, Z. Liu, Z. Feng, C. Wang, Y. Guo, Thermofluid field of molten pool and its effects during selective laser melting (SLM) of Inconel 718 alloy, *Additive Manufacturing*, **21**, 567-578 (2018)
31. W.E. King, H.D. Barth, V.M. Castillo, G.F. Gallegos, J.W. Gibbs, D.E. Hahn, C. Kamath, A.M. Rubenchik, Observation of keyhole-mode laser melting in laser powder-bed fusion additive manufacturing, *Journal of Materials Processing Technology*, **214**(12), 2915-2925 (2014)
32. H. Wang, L. Wang, R. Cui, B. Wang, L. Luo, Y. Su, Differences in microstructure and nano-hardness of selective laser melted Inconel 718 single tracks under various melting modes of molten pool, *Journal of Materials Research and Technology*, **9**(5), 10401-10410 (2020)
33. G.A. Rao, M. Kumar, M. Srinivas, D.S. Sarma, Effect of standard heat treatment on the microstructure and mechanical properties of hot isostatically pressed superalloy inconel 718, *Materials Science and Engineering: A*, **355**(1-2), 114-125 (2003)
34. K.N. Amato, S.M. Gaytan, L.E. Murr, E. Martinez, P.W. Shindo, J. Hernandez, S. Collins, F. Medina, Microstructures and mechanical behavior of Inconel 718 fabricated by selective laser melting, *Acta Materialia*, **60**(5), 2229-2239 (2012)
35. D. Zhang, Z. Feng, C. Wang, W. Wang, Z. Liu, W. Niu, Comparison of microstructures and mechanical properties of Inconel 718 alloy processed by selective laser melting and casting, *Materials Science and Engineering: A*, **724**, 357-367 (2018)
36. T.G. Gallmeyer, S. Moorthy, B.B. Kappes, M.J. Mills, B. Amin-Ahmadi, A.P. Stebner, Knowledge of process-structure-property relationships to engineer better heat treatments for laser powder bed fusion additive manufactured Inconel 718, *Additive Manufacturing*, **31**, 100977 (2020)
37. P. Mohanty, J. Mazumder, Solidification behavior and microstructural evolution during laser beam—material interaction, *Metallurgical and materials transactions B*, **29**(6), 1269-1279 (1998)
38. J. Kroos, U. Gratzke, M. Vicanek, G. Simon, Dynamic behaviour of the keyhole in laser welding, *Journal of Physics D: Applied Physics*, **26**, 481 - 486 (1992)
39. A. Matsunawa, J.-D. Kim, N. Seto, M. Mizutani, S. Katayama, Dynamics of keyhole and molten pool in laser welding, *Journal of Laser Applications*, **10**(6), 247-254 (1998)
40. H. Zhao, W. Niu, B. Zhang, Y. Lei, M. Kodama, T. Ishide, Modelling of keyhole dynamics andporosity formation considering theadaptive keyhole shape and three-phasecoupling during deep-penetration laserwelding, *Journal of Physics D: Applied Physics*, **44**, (2011)
41. T. Qi, H. Zhu, H. Zhang, J. Yin, L. Ke, X. Zeng, Selective laser melting of Al7050 powder: Melting mode transition and comparison of the characteristics between the keyhole and conduction mode, *Materials & Design*, **135**, 257-266 (2017)
42. G.V. De Leon Nope, L.I. Perez-Andrade, J. Corona-Castuera, D.G. Espinosa-Arbelaez, J. Muñoz-Saldaña, J.M. Alvarado-Orozco, Study of volumetric energy density limitations on the IN718 mesostructure and microstructure in laser powder bed fusion process, *Journal of Manufacturing Processes*, **64**, 1261-1272 (2021)
43. H. Hyer, L. Zhou, S. Park, G. Gottsfritz, G. Benson, B. Tolentino, B. McWilliams, K. Cho, Y. Sohn, Understanding the laser powder bed fusion of AlSi10Mg alloy, *Metallography, Microstructure, and Analysis*, **9**(4), 484-502 (2020)

44. T. Abu-Lebdeh, R. Damptey, V. Lamberti, S. Hamoush, Powder Packing Density and Its Impact on SLM-Based Additive Manufacturing, The Minerals, Metals & Materials Society, 2019, Springer International Publishing, pp 355-367
45. Y. Shi, Y. Zhang, Simulation of random packing of spherical particles with different size distributions, *Applied Physics A*, **92**(3), 621-626 (2008)
46. D. Rosenthal, The theory of moving source of heat and its application to metal treatment, *Transactions ASME*, **43**(11), 849 - 866 (1946)
47. J. Sweet, E. Roth, M. Moss, Thermal conductivity of Inconel 718 and 304 stainless steel, *International journal of thermophysics*, **8**(5), 593-606 (1987)
48. H. Ki, J. Mazumder, P.S. Mohanty, Modeling of laser keyhole welding: Part II. Simulation of keyhole evolution, velocity, temperature profile, and experimental verification, *Metallurgical and Materials Transactions A*, **33**(6), 1831-1842 (2002)
49. T.-N. Le, Y.-L. Lo, Z.-H. Lin, Numerical simulation and experimental validation of melting and solidification process in selective laser melting of IN718 alloy, *Additive Manufacturing*, **36**, 101519 (2020)
50. C.-C. Tseng, C.-J. Li, Numerical investigation of interfacial dynamics for the melt pool of Ti-6Al-4V powders under a selective laser, *International Journal of Heat and Mass Transfer*, **134**, 906-919 (2019)
51. S.A. Khairallah, A. Anderson, Mesoscopic simulation model of selective laser melting of stainless steel powder, *Journal of Materials Processing Technology*, **214**(11), 2627-2636 (2014)
52. W. Yan, W. Ge, Y. Qian, S. Lin, B. Zhou, W.K. Liu, F. Lin, G.J. Wagner, Multi-physics modeling of single/multiple-track defect mechanisms in electron beam selective melting, *Acta Materialia*, **134**, 324-333 (2017)
53. M. Bayat, S. Mohanty, J.H. Hattel, Multiphysics modelling of lack-of-fusion voids formation and evolution in IN718 made by multi-track/multi-layer L-PBF, *International Journal of Heat and Mass Transfer*, **139**, 95-114 (2019)
54. H.J. Willy, X. Li, Z. Chen, T.S. Herng, S. Chang, C.Y.A. Ong, C. Li, J. Ding, Model of laser energy absorption adjusted to optical measurements with effective use in finite element simulation of selective laser melting, *Materials & Design*, **157**, 24-34 (2018)
55. T.Z. Kattamis, J.M. Coughlin, M.C. Flemings, Influence of coarsening on dendrite arm spacing of aluminum copper alloys, *Transactions ASME*, **239**, 1504 (1967)
56. L. Ling, Y. Han, W. Zhou, H. Gao, D. Shu, J. Wang, M. Kang, B. Sun, Study of microsegregation and Laves phase in Inconel718 superalloy regarding cooling rate during solidification, *Metallurgical and Materials Transactions A*, **46**(1), 354-361 (2015)
57. M. Tang, P.C. Pistorius, S. Narra, J.L. Beuth, Rapid solidification: selective laser melting of AlSi10Mg, *Jom*, **68**(3), 960-966 (2016)
58. G. Pottlacher, H. Hosaeus, E. Kaschnitz, A. Seifter, Thermophysical properties of solid and liquidInconel 718 alloy, *Scandinavian Journal of Metallurgy*, **31**(3), 161-168 (2002)
59. T. Vilaro, C. Colin, J.-D. Bartout, L. Nazé, M. Sennour, Microstructural and mechanical approaches of the selective laser melting process applied to a nickel-base superalloy, *Materials Science and Engineering: A*, **534**, 446-451 (2012)
60. S. Kou, Welding metallurgy, 3rd ed., Wiley, 2020

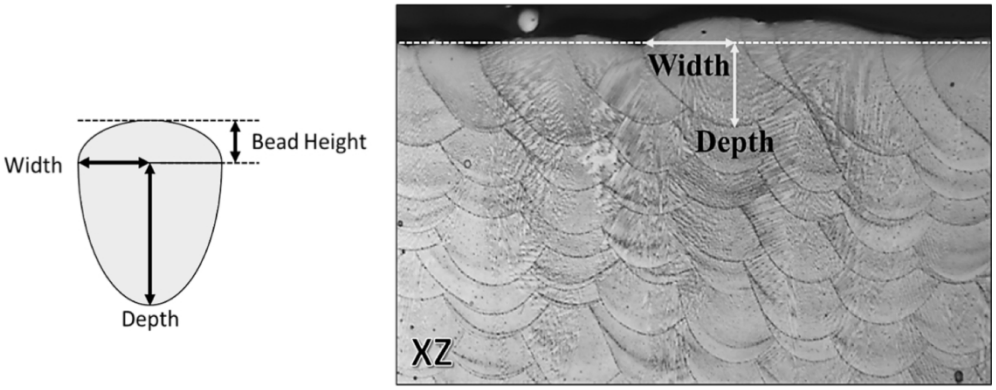


Figure 1: A schematic and representative optical micrograph of melt pools showing lateral symmetry. Note that the actual melt pool width is twice that of measured width indicated.

152x58mm (300 x 300 DPI)

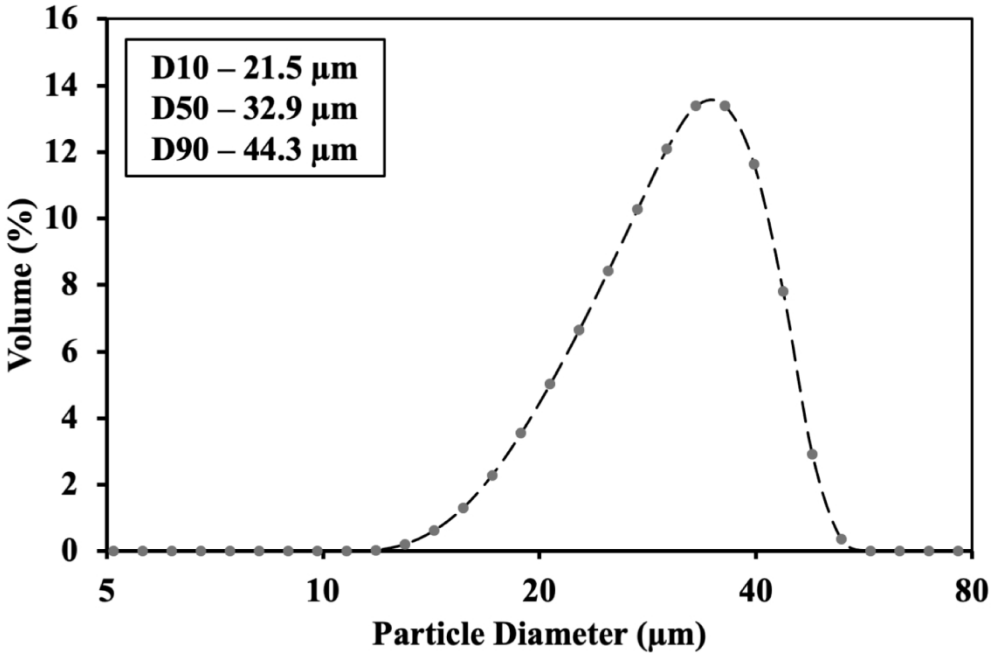


Figure 2: Particle size distribution of as-received IN718 powder feedstock.

152x99mm (300 x 300 DPI)

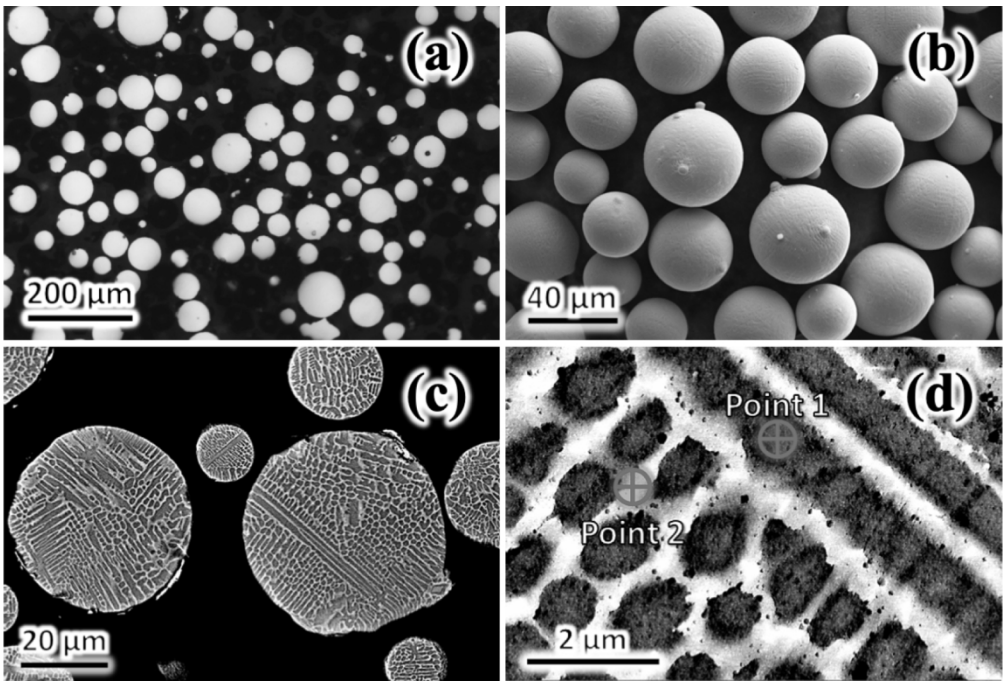


Figure 3: (a) Optical micrograph of unetched IN718 powder cross section, (b) secondary electron (SE) micrograph of IN718 powder, (c) backscatter electron (BSE) micrograph of IN718 powder, (d) cellular-dendritic microstructural details in BSE micrograph.

152x102mm (300 x 300 DPI)

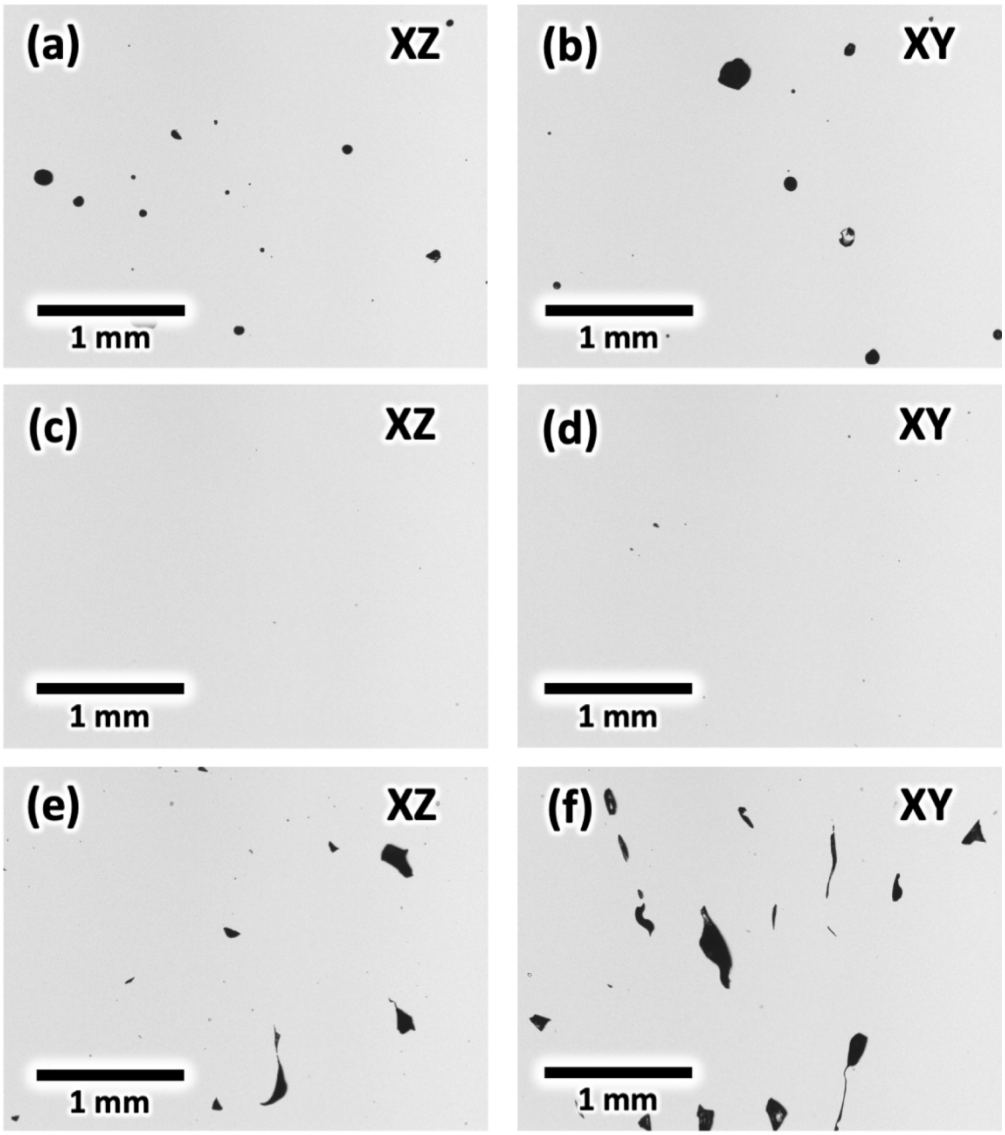


Figure 4: Optical micrographs from IN718 exhibiting (a,b) keyhole pores, (c,d) full density and (e,f) lack of fusion flaws from the (a,c,e) XZ and (b,d,f) XY cross sections. These samples fabricated with varying laser scan speed while power (275 W) hatch spacing (120 μm), and slice thickness (30 μm) were kept constant.

152x172mm (300 x 300 DPI)

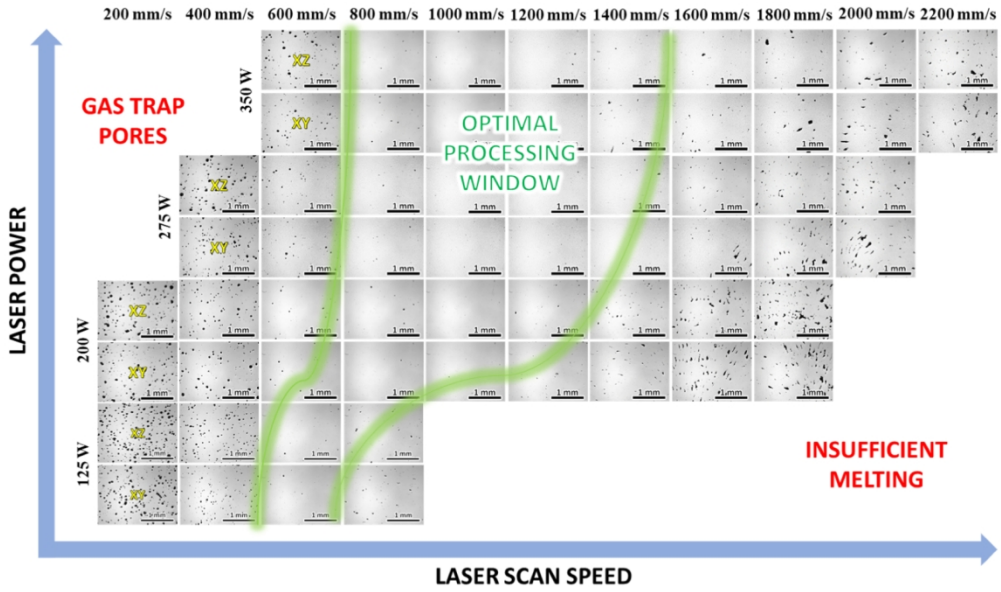


Figure 5: Optical micrographs of XZ and XY cross sections of IN718 samples produced with varying laser power and laser scan speed, while hatch spacing (120 µm), and slice thickness (30 µm) were kept constant.

152x89mm (300 x 300 DPI)

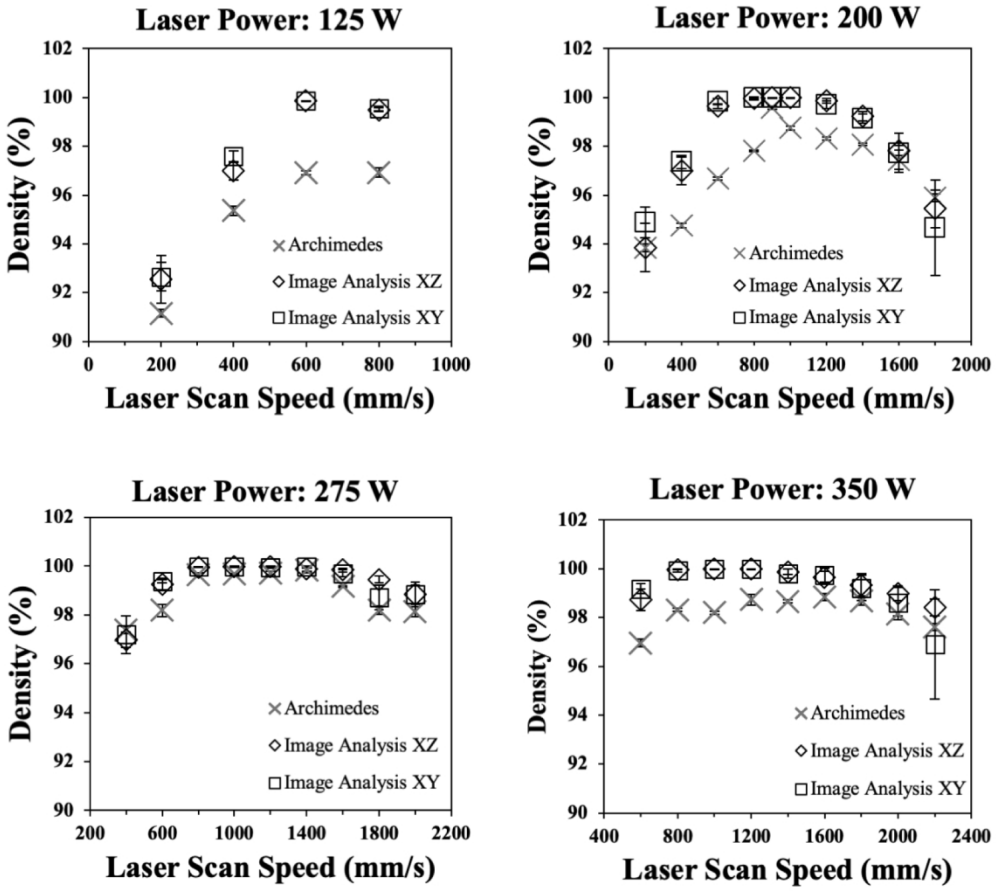


Figure 6: Relative sample density as a function of laser scan speeds at constant hatch spacing and slice thickness of 120 μm and 30 μm, respectively, for laser power of (a) 125 W; (b) 200 W; (c) 275 W; and (d) 350 W.

152x136mm (300 x 300 DPI)

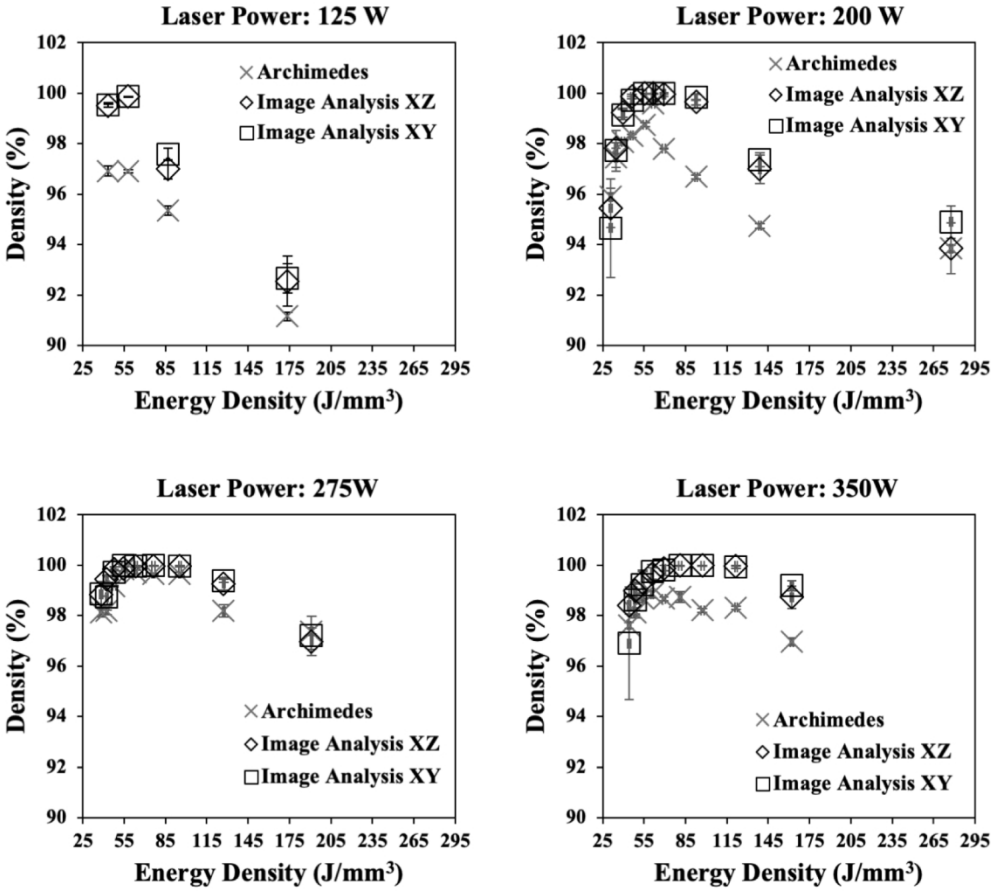


Figure 7: Relative sample density as a function of energy density at hatch spacing, slice thickness, and scan rotation angle of 120 μm, 30 μm, and 16°, respectively, for laser power of (a) 125 W; (b) 200 W; (c) 275 W; and (d) 350 W.

152x135mm (300 x 300 DPI)

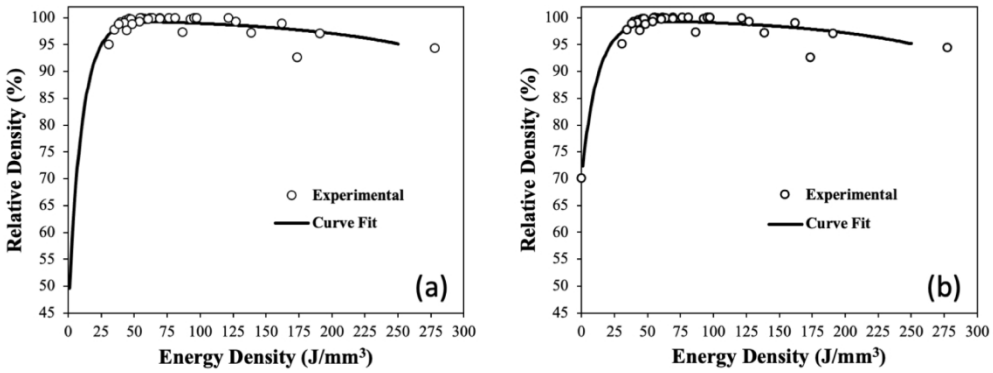


Figure 8: Predicted and experimental relative densities as a function of energy density (a) without and (b) with density (e.g., powder packing) of 70 % corresponding to zero energy density.

152x56mm (300 x 300 DPI)

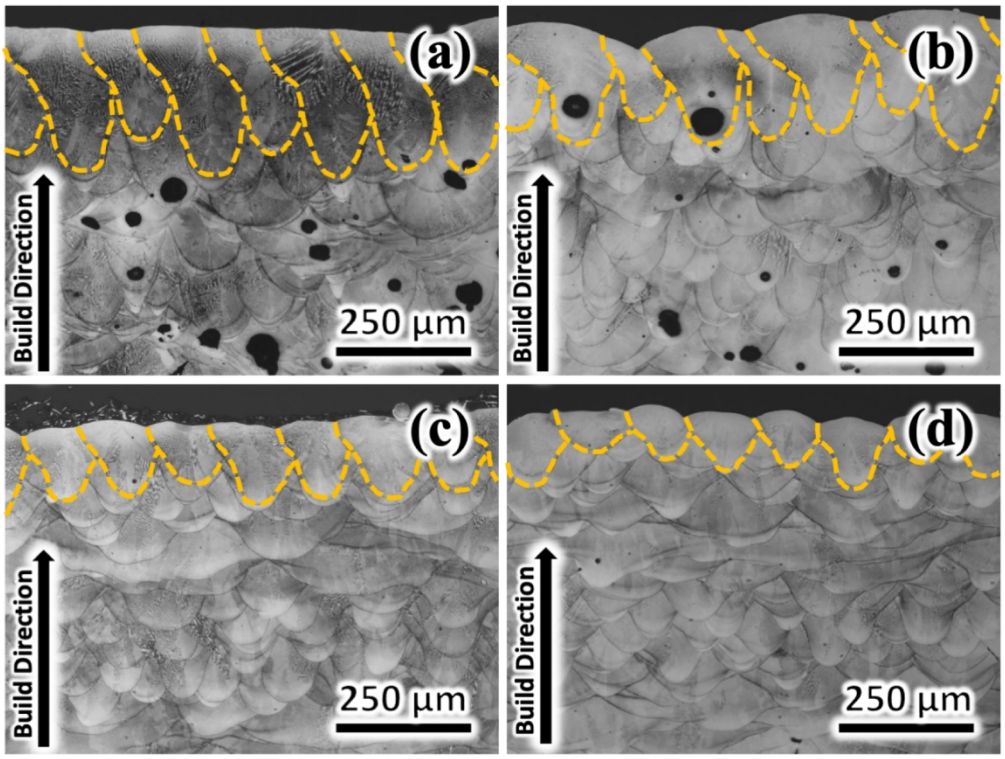


Figure 9: Melt pools observed parallel to the build direction at scan speeds of: (a) 200 mm/s, (b) 400 mm/s, (c) 600 mm/s, (d) 800 mm/s. Laser power, hatch spacing, slice thickness, and scan rotation angle were constant at 125W, 120 µm, 30 µm, and 16°, respectively.

152x114mm (300 x 300 DPI)

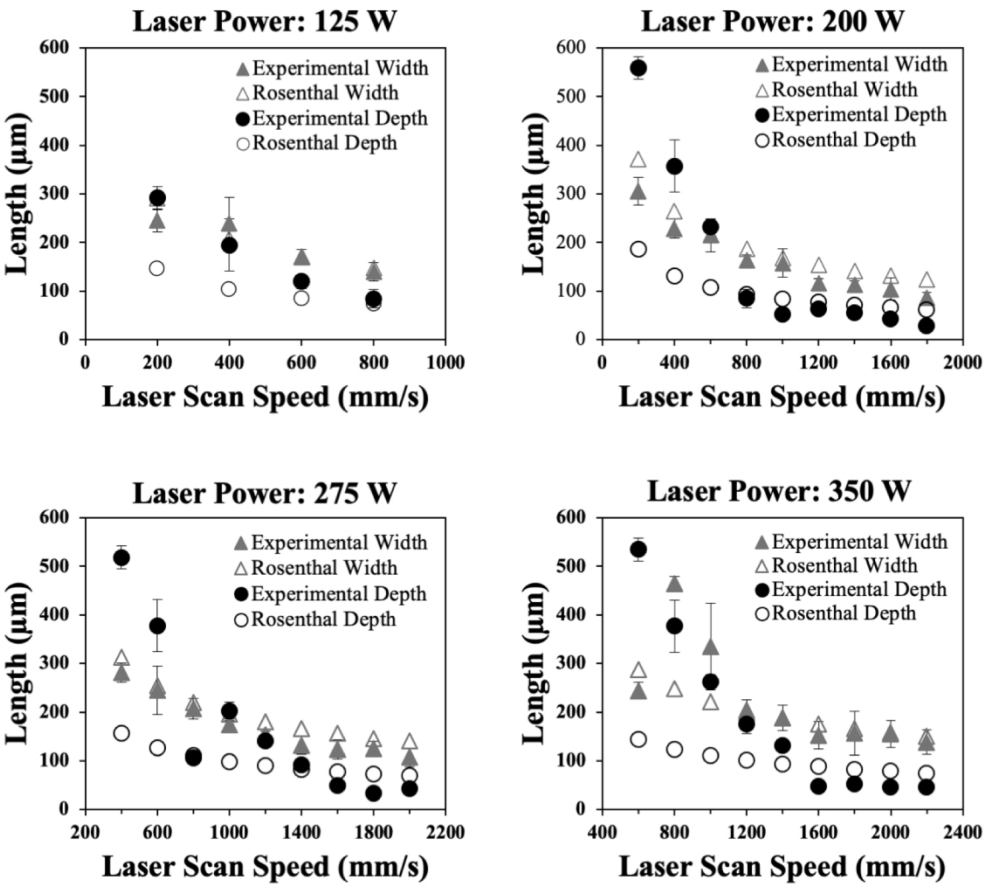


Figure 10: Melt pool dimensions experimentally measured and predicted by Rosenthal's equation as a function of laser scan speed at constant hatch spacing, slice thickness, and scan rotation angle of 120 μm, 30 μm, and 16°, respectively, for laser power of (a) 125 W; (b) 200 W; (c) 275 W; and (d) 350 W.

152x135mm (300 x 300 DPI)

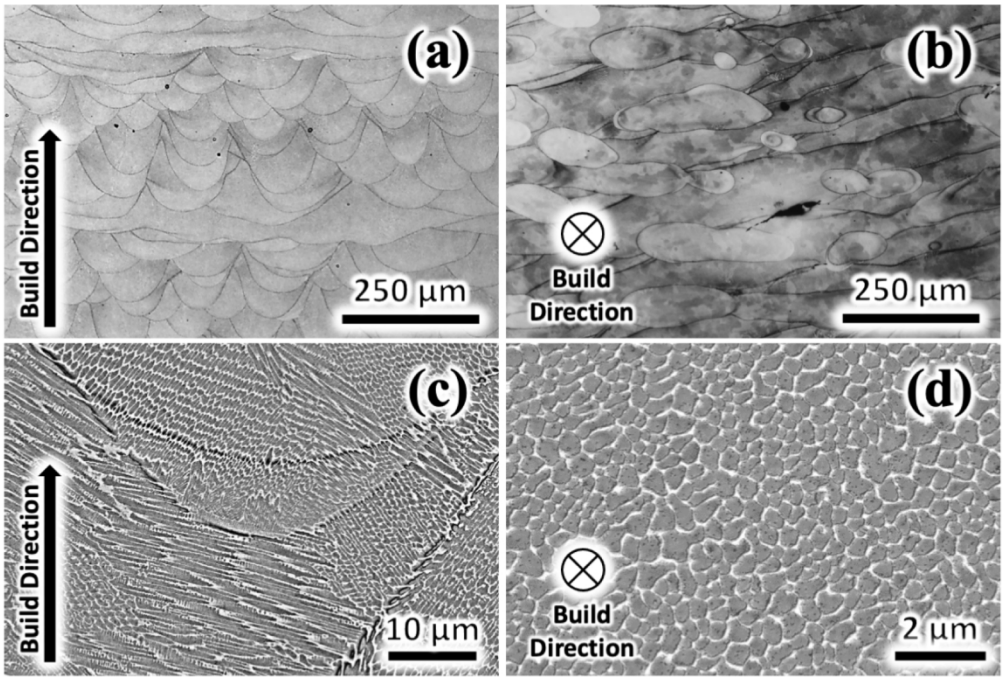


Figure 11: Optical micrographs of SLMed IN718 obtained (a) parallel to the build direction and (b) perpendicular to the build direction. Backscatter electron micrographs of SLMed IN718 (c) parallel to the build direction and (b) perpendicular to the build direction. Laser power, laser scan speed, hatch spacing, slice thickness, and scan rotation angle were constant at 125 W, 800 mm/s, 120 µm, 30 µm, and 16°, respectively.

152x102mm (300 x 300 DPI)

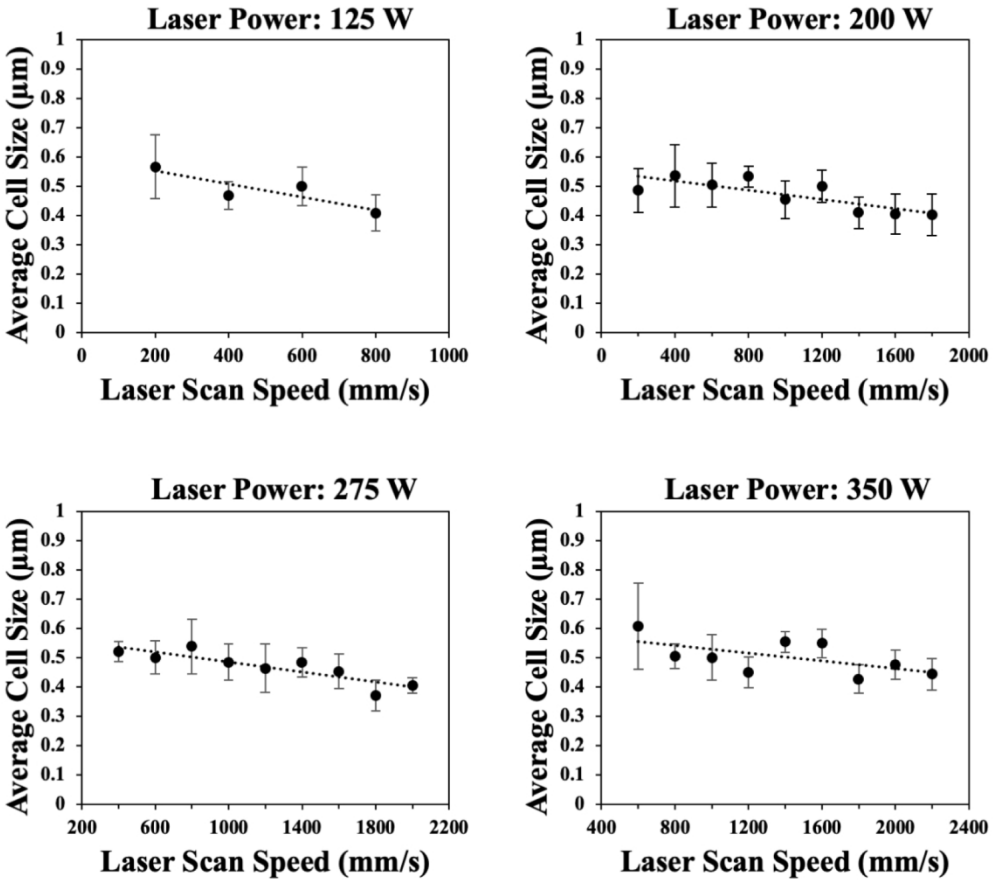


Figure 12: Variation in average cell size as a function of laser scan speed. Laser power, hatch spacing, slice thickness, and scan rotation angle were held constant at 125 W, 120 µm, 30 µm, and 16°, respectively, for laser power of (a) 125 W; (b) 200 W; (c) 275 W; and (d) 350 W.

152x134mm (300 x 300 DPI)

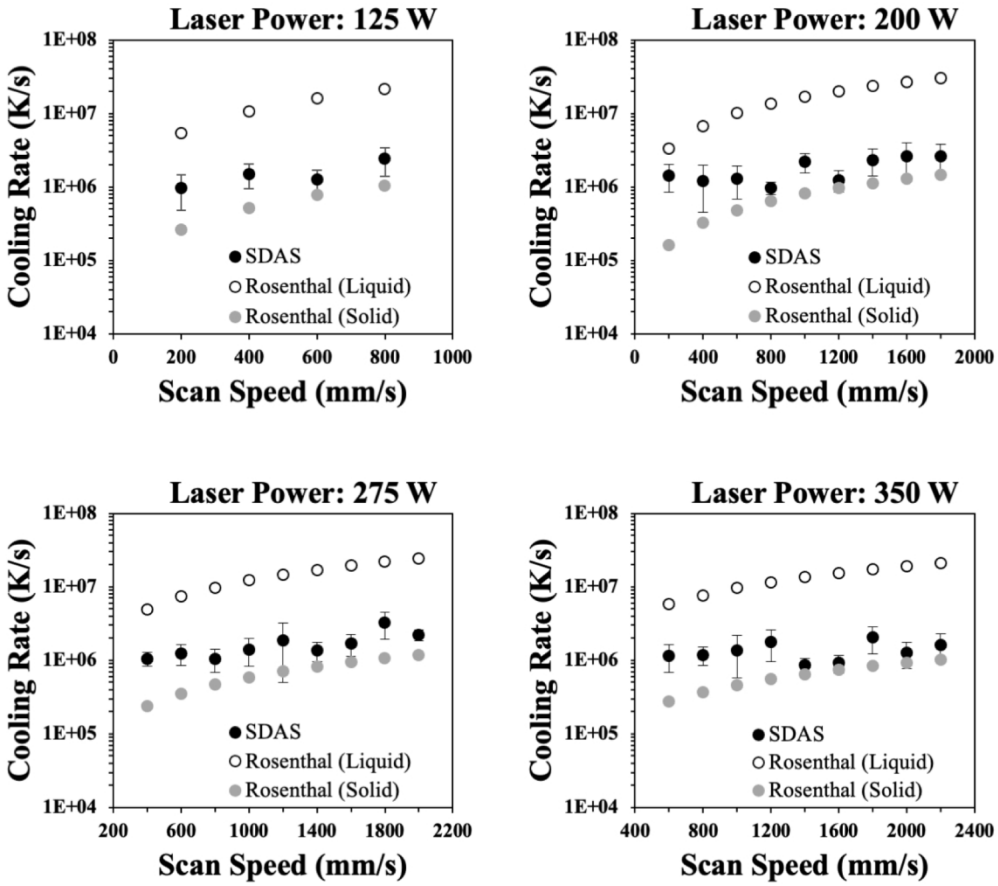


Figure 13: Comparison between SDAS and Rosenthal cooling rates at varying laser powers and scan speeds at constant hatch spacing, slice thickness, and scan rotation angle of 120 μm, 30 μm, and 16°, respectively, for laser power of (a) 125 W; (b) 200 W; (c) 275 W; and (d) 350 W.

152x134mm (300 x 300 DPI)

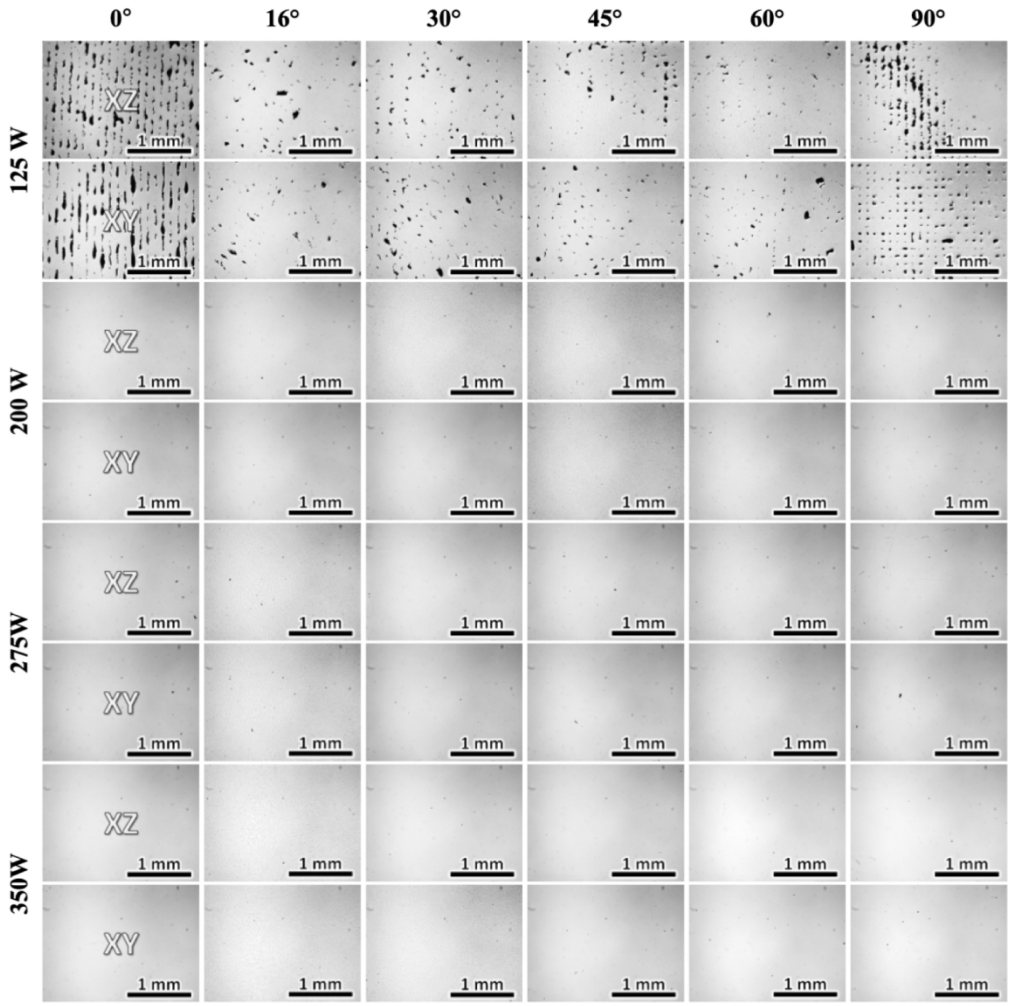


Figure 14: Optical micrographs from IN718 samples produced as functions of laser power and scan rotation angle. The other parameters, laser scan speed, hatch spacing, and slice thickness were kept constant at 900 mm/s, 120 μm, 30 μm, respectively.

152x152mm (300 x 300 DPI)

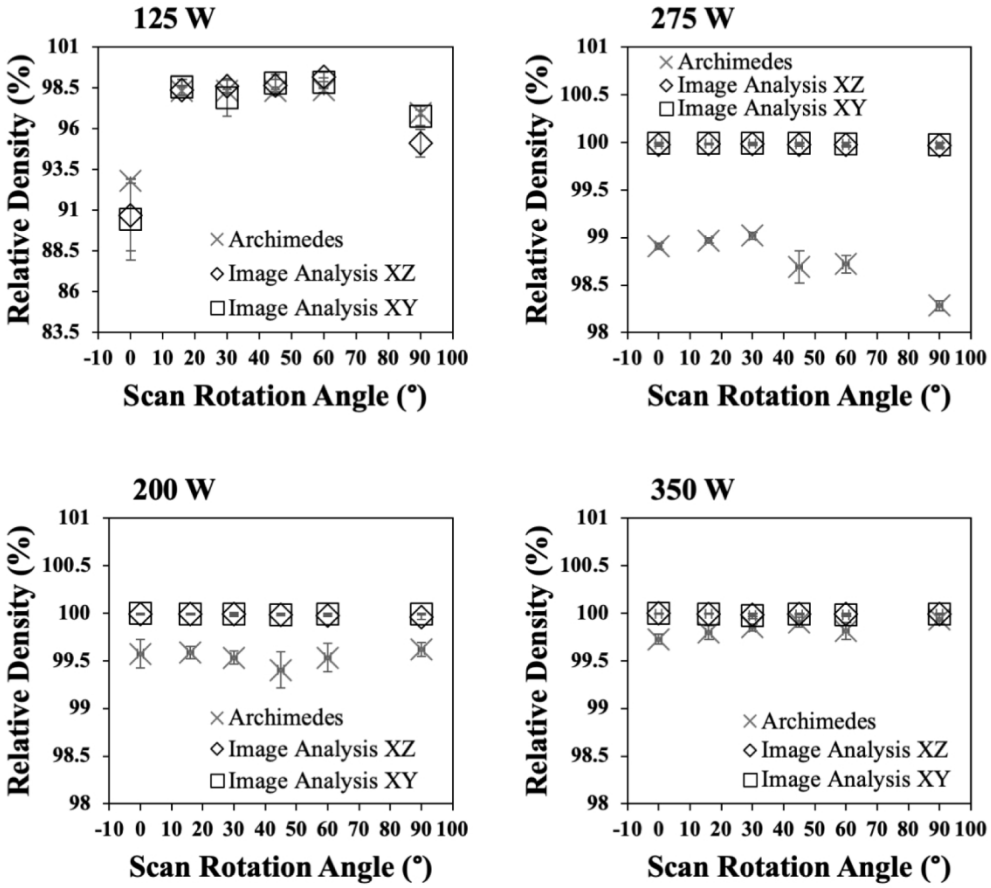


Figure 15: Relative density as a function of laser scan rotation angles at laser power of (a) 125 W; (b) 200 W; (c) 275 W; and (d) 350 W. Scan speed, hatch spacing, and slice thickness were held constant at 900 mm/s, 120 μm, and 30 μm, respectively.

152x135mm (300 x 300 DPI)

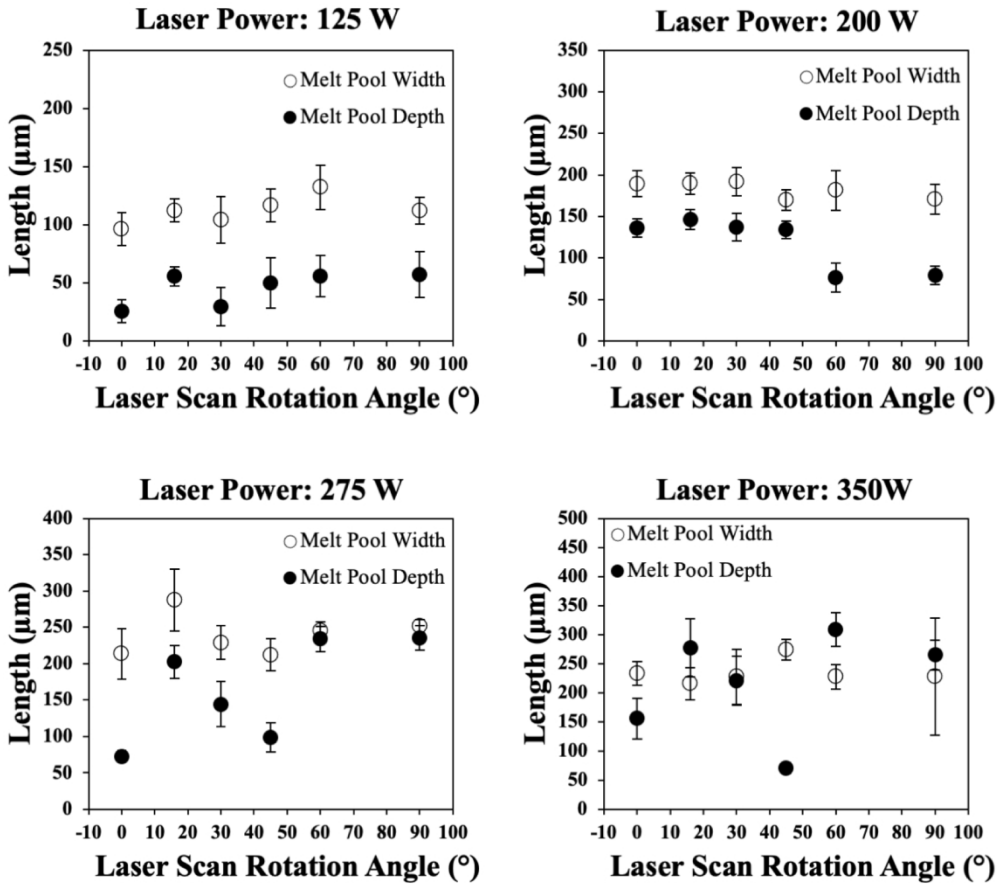


Figure 16: Melt pool dimensions as a function of laser scan rotation angles at laser power of (a) 125 W; (b) 200 W; (c) 275 W; and (d) 350 W. Scan speed, hatch spacing, and slice thickness were held constant at 900 mm/s, 120 µm, and 30 µm, respectively.

152x134mm (300 x 300 DPI)

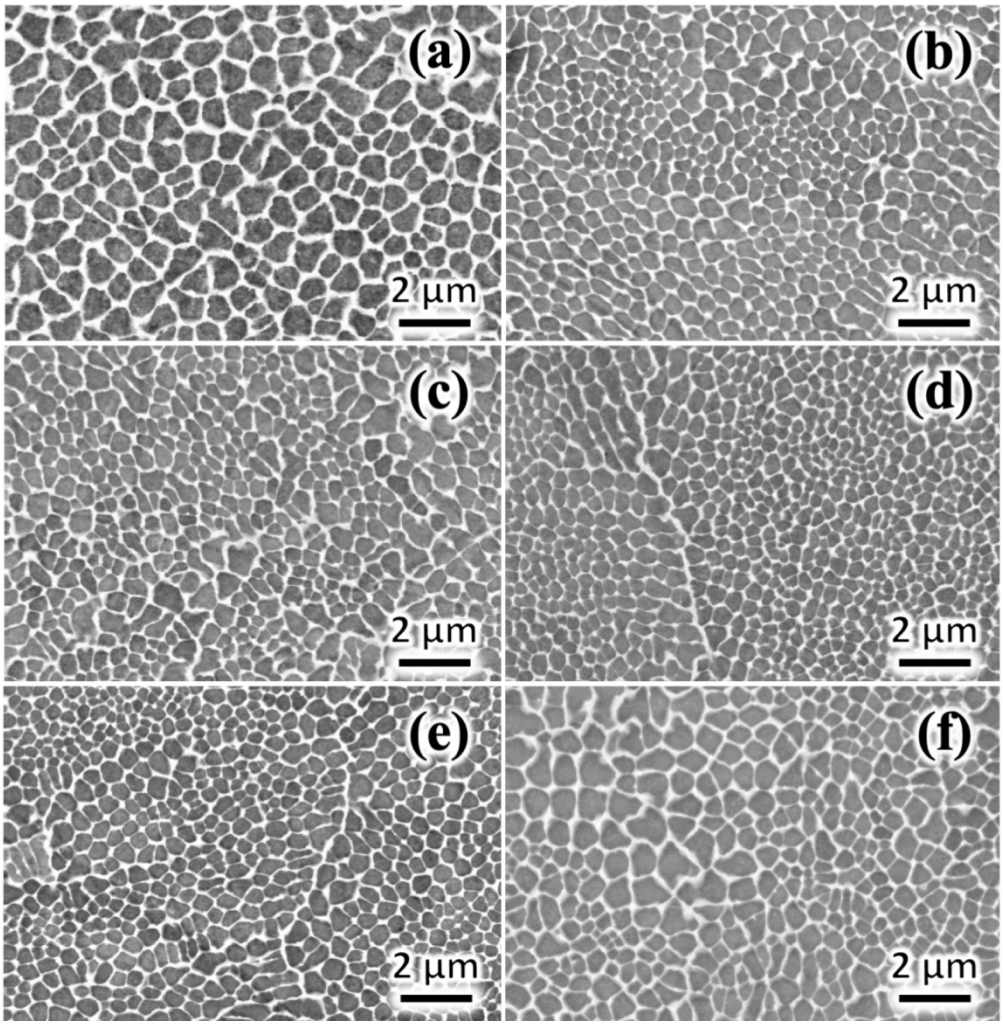


Figure 17: BSE micrographs showing cellular microstructure observed perpendicular to the build direction as a function of laser scan rotation angle of (a) 0°, (b) 16°, (c) 30°, (d) 45°, (e) 60°, and (f) 90°. Laser power, scan speed, hatch spacing, and slice thickness were held constant at 125 W, 900 mm/s, 120 µm, and 30 µm, respectively.

152x154mm (300 x 300 DPI)

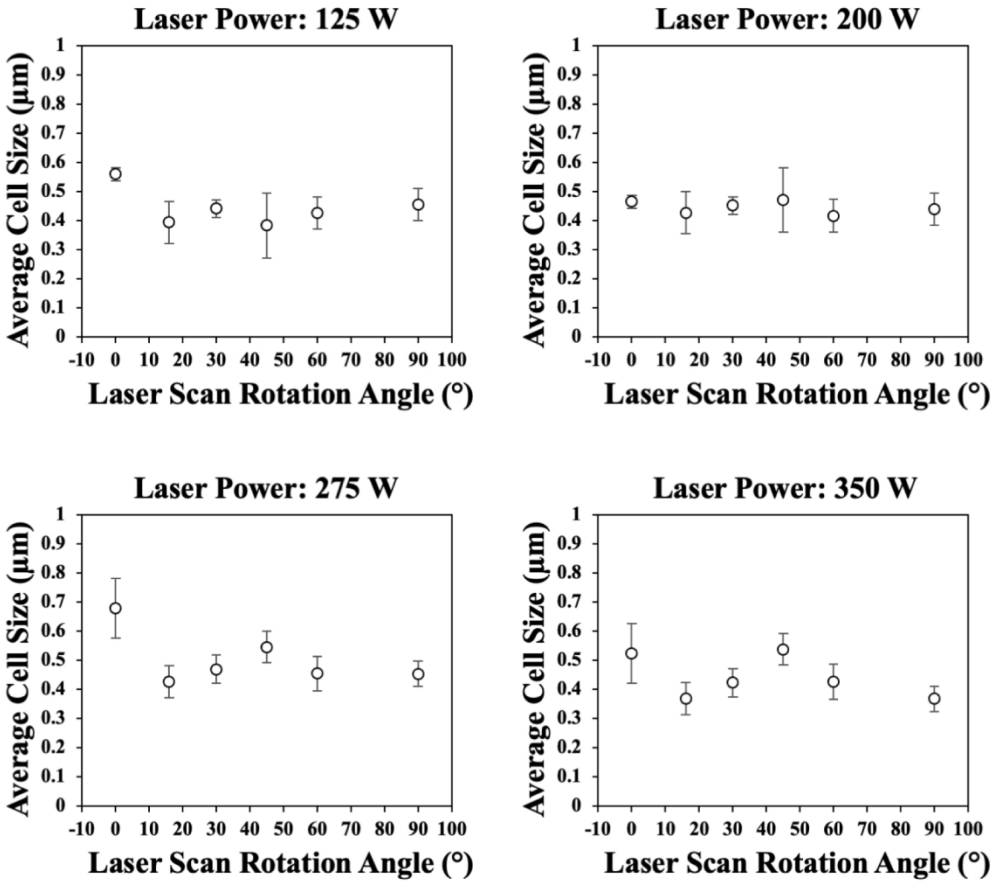


Figure 18: Average cell size as a function of laser scan rotation angles at laser power of (a) 125 W; (b) 200 W; (c) 275 W; and (d) 350 W. Scan speed, hatch spacing, and slice thickness were held constant at 900 mm/s, 120 µm, and 30 µm, respectively.

152x134mm (300 x 300 DPI)

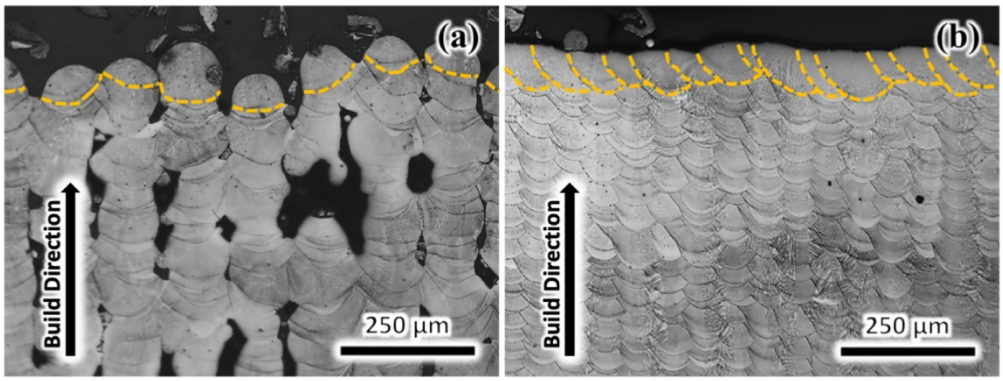


Figure 19: Optical micrographs of XZ cross section with laser power, scan speed, and slice thickness of 125 W, 900 mm/s, 30 µm, respectively, at hatch spacing: (a) 120 µm, (b) 60 µm.

152x57mm (300 x 300 DPI)

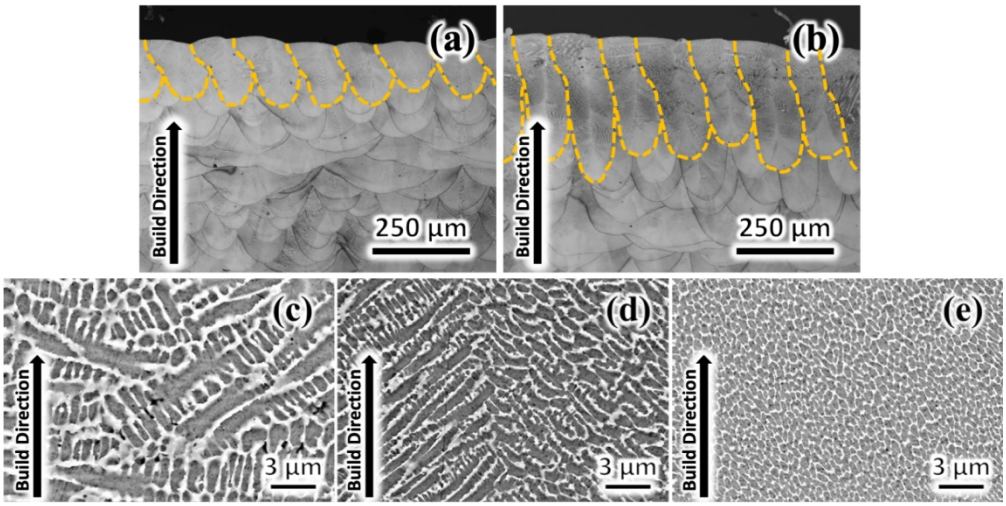


Figure 20: Melt pool comparison between (a) 200 W and (b) 350 W at scan rotation angle, scan speed, hatch spacing, and slice thickness of 16°, 900 mm/s, 120 µm, and 30 µm, respectively. The cell size within deep melt pools observed in (b): (c) near melt pool surface, (d) middle of melt pool, (e) near the bottom of melt pool.

152x76mm (300 x 300 DPI)